Tissue Stabilization in MRI-Guided Breast Biopsy

TISSUE STABILIZATION IN MRI-GUIDED BREAST BIOPSY

BY

BEHZAD IRANPANAH, B.Sc.

A THESIS
SUBMITTED TO THE DEPARTMENT OF BIOMEDICAL ENGINEERING
AND THE SCHOOL OF GRADUATE STUDIES
OF MCMASTER UNIVERSITY
IN PARTIAL FULFILMENT OF THE REQUIREMENTS
FOR THE DEGREE OF
MASTER OF APPLIED SCIENCE

Master of Applied Science (2013)
(Biomedical Engineering)

McMaster University
Hamilton, Ontario, Canada

TITLE:	Tissue Stabilization in MRI-Guided Breast Biopsy
AUTHOR:	Behzad Iranpanah B.Sc., (Mechanical Engineering) Sharif University of Technology, Tehran, Iran
SUPERVISOR:	Dr. Shahin Sirouspour, Dr. Alexandru Patriciu
NUMBER OF PAGES:	xiv, 88

To my beloved parents and

my darling wife

Abstract

Breast cancer is the most common form of cancer in women in the United States. Histopathological examination through breast biopsy is considered as the “Gold Standard” for a definitive diagnosis. Contrast-enhanced Magnetic Resonance Imaging (MRI) is often used for guiding the biopsy in those cases in which the tumor may not be detectable under Ultrasound or X-ray mammography. Stabilization of the breast tissue during the biopsy is critical for its success to ensure that the target would not be displaced due to the patient movement or tissue deformation. Conventionally, the breast tissue is immobilized by firmly compressing it between two parallel plates. However, high compression forces causes significant patient discomfort and can reduce the intake of the contrast agent, which negatively impact the image quality.

This thesis introduces devices and control methodologies for active tissue stabilization in magnetic resonance imaging (MRI)-guided breast biopsy. Pneumatic and piezoelectric actuators have been considered for developing concept designs for MRI-compatible tissue stabilization devices. Only the pneumatic device has been prototyped and tested. The device is comprised of two pneumatically-actuated support plates that would stabilize the biopsy target movements during needle insertion. An optimized geometry for the support plates allows for a good degree of tissue stabilization without relying on large compression forces. The plate configuration can also be adjusted inside the magnet bore using pneumatic actuators driven by pressure-controlled valves that are placed in the MR control room. This capability allows for the compensation of the target displacement based on MR image feedback. When combined with a separate needle drive mechanism, this stabilization device would enable in-bore MR-guided breast biopsy in combination with an in-bore needle driver system. The proposed approach offers improved target stabilization at reduced compression force and patient discomfort, that may also enhance MR image quality as result of greater intake of contrast agent. The open-front design of the stabilization plates provides greater flexibility in selecting the needle insertion entry point, and active adjustment of the support plates based on MR feedback improves the targeting accuracy.

A concept design for a MR-compatible needle driver mechanism using piezoelectric actuators is also proposed. Experiments performed on chicken breast tissue with a prototype of the device demonstrate the effectiveness of this mechanism in increasing needle targeting accuracy using two simple error correction strategies. Furthermore, MRI compatibility tests are carried out to asses the performance of the device inside MRI.

Acknowledgements

Foremost, I would like to express my sincerest appreciation to my supervisors, Dr. Shahin Sirouspour and Dr. Alexandru Patriciu, for their encouragement, support and invaluable comments throughout my studies at McMaster University. I am deeply grateful to Dr. Michael D. Noseworthy for providing us the access to the MRI machine at Imaging Research Center at St. Joseph's Healthcare and for his priceless suggestions.

I would like to acknowledge the support of the Center for Surgical Invention and Innovation (CSii) for a part of this work related to the design and optimization of a passive prototype of the tissue stabilization device.

My appreciation to my colleagues in the Haptics, Telerobotics and Computational Vision Laboratory for making an amazing place to study. Special thanks to Maggie Chen for her impressive work in designing the stabilization plate and for helping me during the long experiments. My kind regards to my dear friends, Saman Rahnamaei and Sajad Salmanipour for their incredible intellectual supports, suggestions and patience. Much thanks to Tyler Ackland for his unbelievable help and valuable time with all my questions and requests in the past year.

Thanks are due to Morteza Azimifar and my friends in Hamilton who made my stay in Hamilton enjoyable.

Special thanks to my family for their endless love and for always supporting me through my life.

Last but not the least, my heartfelt appreciation goes to Rojin for her love, kindness, and for always cheering me up.

Notation and abbreviations

FNA	Fine Needle Aspiration
CB	Core Biopsy
VAB	Vacuum Assisted Biopsy
MRI	Magnetic Resonance Imaging
DCIS	Ductal Carcinoma in Situ
DOF	Degree of Freedom
SNR	Signal to Noise Ratio
CAD	Computer Aided Design
PID	Proportional Integral Derivative
SPGR	Spoiled Gradient Echo
RF	Radio Frequency

Contents

List of Figures

Chapter 1

Introduction and Problem Statement

1.1 Motivation

Breast cancer is one the most common cancers and the second leading cause of death among women in the United States (Society, 2007). Early detection of malignant lesions in women with high risk of developing breast cancer is crucial, as it can lead to a 100% survival rate (Goldfischer, 2010). Improvements in accuracy of non-operative diagnosis with needle biopsy over the years have eliminated the necessity of performing open surgical biopsies (O'Flynn *et al.*, 2010). Biopsy is performed to determine existence and characteristics of a suspected lesion . Fine needle aspiration (FNA), core biopsy (CB), and vacuum assisted biopsy (VAB) are the three types of lesion sampling with the VAB being the most commonplace method nowadays.

Currently, X-Ray Mammography and Ultrasound-guided breast biopsy are the clinical standard of practice to examine suspicious breast lesions as they can help detect and identify most lesions (Mushlin *et al.*, 1998; Harvey *et al.*, 2000). However, there are some lesions which can be missed by these modalities but are detectable under Magnetic Resonance Imaging (MRI), because of its higher sensitivity (Goldfischer, 2010; LaTrenta *et al.*, 2003). MRI is known to be effective in diagnosing ductal carcinoma in situ (DCIS) and cancer in contralateral breast (Lehman *et al.*, 2007; Kuhl *et al.*, 2007). MRI has no ionizing radiation or other known safety hazards. Moreover, MRI allows for dynamic adjustment of imaging plane and volumes to follow movements of a MR-compatible robotic device to enable robot-assisted biopsy (Debatin and Adam, 1998; Christoforou *et al.*, 2007). Studies in (Podo *et al.*, 2002; Warner *et al.*, 2001; Kuhl *et al.*, 2000) reported higher sensitivity (86% to 100%) of MRI in tumor detection compared to ultrasound and mammography; however, they also reveal one of the main disadvantages of MRI, i.e. the lack of specificity (37% to 97%) (Morris *et al.*, 2005). Malignant and benign lesions cannot be easily distinguished based on images only (Plewes *et al.*, 2000); biopsy of suspicious lesions is necessary for a definitive diagnosis (Morris *et al.*, 2005). Cost, variation in techniques and interpretations, and limited capabilities of MRI biopsy devices have contributed to slow adoption of this screening techniques. However, improvements in techniques and technology are expected to lead to wider adoption of MRI in breast cancer diagnosis to benefit women in high risk of developing breast cancer.

In conventional MRI-guided breast biopsy, the patient lies pone on a table and her breast is immobilized by firmly compressing it between two parallel plates. The patient is then moved inside the magnet bore and contrast enhanced images of breast are acquired; the images are used to estimate the location of the lesion. The best grid hole for the biopsy needle insertion and the depth of the lesion are determined based on the location of the suspicious lesion. The patient is then moved out of the magnet and a MRI-compatible needle placeholder, known as obturator, is inserted to reach the target location under local anaesthesia of the breast. Prior to sampling the tissue, another MR image is usually acquired to confirm proper placement of the obturator, requiring another transfer of the patient in and out of the machine. Finally, the obturator is replaced with a biopsy gun and the tissue sample is obtained outside the magnet via an aperture slightly above the needle tip. Another MR image is usually acquired to confirm proper extraction of the lesion (Morris *et al.*, 2005; Yang *et al.*, 2011b; Liberman *et al.*, 2003).

Injection of contrast agents such as gadolinium enhance the tumor target visibility on MR images. Higher vascularization of the lesions in comparison to normal tissue, results in greater uptake of contrast agent in those areas, making them enhanced in the MR image (Goldfischer, 2010). However, this effect is temporary as the lesions are only visible immediately after the contrast agent uptake. Therefore, upon localization of the target, the breast tissue needs to be completely immobilized throughout the procedure to prevent target dislocations due to patient movement or needle insertion forces. This is a crucial step to prevent damage to healthy tissue and ensure successful sample extraction as the median lesion size is only 1 cm (Liberman *et al.*, 2003; Debatin and Adam, 1998; Pfleiderer *et al.*, 2005; Krieger *et al.*, 2005; Pfleiderer *et al.*, 2003). Deurloo *et al.* (2001) discovered that tissue and needle displacements accounted for a total of 2.4 mm positioning error in breast biopsy. Positioning errors may also force multiple biopsy attempts to confirm accurate placement of the tool, which can further lengthen the procedure (Lufkin, 1999).

To reduce target movements, the breast tissue is usually immobilized using highly compressed parallel plates. However, high compression forces cause significant patient discomfort, dramatic distortion of the lesion shape in the MR images, and can reduce the uptake of the contrast agent, which would degrade the image quality (Azar *et al.*, 2002). Moreover, parallel plates used to immobilize the tissue restrict the needle entry point to a limited set of points on a gridded plate; this can cause the insertion to be performed in an angle rather than a direct trajectory (Morris *et al.*, 2005). In future, with the possible integration of robotic systems to perform automated breast biopsy procedure, parallel gridded plates can dramatically reduce robot maneuver capabilities in selecting best available trajectories.

Figure 1.1: Standard compression gridded plate in MRI-guided breast biopsy, adapted from (O'Flynn *et al.*, 2010)

Another challenge in MRI-guided breast biopsy is the length the procedure as the target is only visible for a short period of time. A faster biopsy procedure can increase its success rate since the target would be detectable for a longer course of the procedure, and the patient would undergo less discomfort (Liberman *et al.*, 2003). Several researchers have investigated methods for dealing with tissue movement during soft-tissue biopsy and other limitations of the conventional MRI-guided breast biopsy.

1.2 Problem Statement and Thesis Contributions

The thesis seeks to address some of the limitations associated with the conventional breast stabilization method with highly compressed parallel plates in MRI-guided breast biopsy. It will introduce devices and control methodologies for active stabilization of the biopsy target to improve targeting accuracy and at the same time reduce patient discomfort. The proposed active tissue stabilization device builds on the work by Chen (2013) where a passive device with optimized plate geometry was introduced. The passive device with the optimized support plate shape offers comparable target stabilization with that of parallel plates at reduced compression forces. The lower compression forces would decrease patient discomfort and image artifacts associated with the high compression forces exerted by the parallel plates. Moreover, the open-front configuration of the device allows for a superior-inferior approach in needle insertion. This configuration is particularly suitable for integration with a robotic needle driver mechanism for automated in-bore MRI-guided breast biopsy. The contributions of this thesis are in the development of actuated tissue stabilization devices as well as image-based closed-loop control strategies for active stabilization of the biopsy target.

Pneumatic and piezoelectric actuators have been considered for the MR-compatible tissue stabilization device. Concept designs have been developed for piezoelectric-based device with three active degrees of freedom (DOF) and pneumatic-based device with two active DOF. Only the pneumatic device has been prototyped and tested due to unavailability of a sufficient number of piezoelectric actuators. When used in conjunction with a needle drive mechanism, the pneumatically-actuated tissue stabilization device can help address some of the limitations of the standard MRI-guided breast biopsy procedure. Unlike parallel compression plates, the open-front design of the proposed device gives unrestricted access to the breast tissue for the selection of the needle entry point. The shape of the support plates in this device is designed to minimize axial and lateral displacements of targets inside the breast, without relying on excessively high compression forces. This is achieved through an optimization of the plate geometry that is reported in a separate study (Patriciu *et al.*, 2013; Chen, 2013). Lower compression forces help reduce patient discomfort and increase contrast agent uptake, which could improve image quality. While the support plates are initially positioned manually around the breast tissue, their orientation can be actively controlled after the patient is moved inside the MR magnet. This capability is critical for a couple of reasons. It allows for a change in the plate configurations inside the magnet based on the MR image to ensure that the target is properly aligned with the needle insertion path. This simplifies the design of the needle driver mechanism which at most would require two translational DOF, one for elevation and another for insertion. Any target movement due to needle insertion forces and tissue deformation can also be compensated for using image-feedback based control. This approach would likely cause less tissue stress than steering the needle itself, if the needle driver were to compensate for target movements.

A concept design for a MR-compatible needle driver mechanism using custom-made linear bearings is also proposed. The translation DOFs of the system are equipped with piezoelectric actuators. Using the same actuation method, a concept design for the active tissue stabilization device is also proposed. In this design, aside from the orientation adjustment of the plates, their relative lateral distance can also be actively controlled. In contrast, the pneumatically actuated device can only be passively adjusted along this direction.

Using the proposed active tissue stabilization devices, the current flow of MRI-guided breast biopsy procedure will need to be slightly modified. Patient will remain in the prone position as before; the support plates will move in an inferior-superior direction to push the breast against two preloader bars to hold the breast firmly in place. The system can be combined with an in-bore robotic needle driver mechanism that performs needle insertion in a superior-inferior direction. Therefore, the whole system can be fitted inside cylindrical MRI bore. With the stabilization device in place, a pre-operative MR image is taken to identify target location. Based on that, needle insertion entry point and direction are selected. Another image is taken to confirm the alignment of needle trajectory and the target. In case a misalignment is detected, stabilization plates angle can be accordingly adjusted to correct the misalignment inside the magnet. This would eliminate the need for removing the patient from the MRI magnet in order to correct misalignments between the needle and the target and reduce the overall procedure length and cost of MRI. The device can also intra-operatively correct needle/target misalignments based on MR image feedback.

The tissue stabilization device is designed to be fully MR-compatible so it can operate inside the imaging machine without significantly impacting the image quality. Our design approach is based on this crucial requirement, which affects several aspects of the design such as material selection, size of the device, and actuation mechanism. The device needs to be compact to be fitted in the limited space under patient bed while it produces the required movement and workspace. The actuation method of the device must have minimum effect on MR image quality as any artifact can reduce MRI sensitivity in lesion detection. Pneumatic actuators as well as piezoelectric actuators, if placed properly relative to the imaging region, can safely operate inside the magnetic field. Therefore, plate adjustment mechanism is pneumatically actuated using long transmission lines that supply the required air from MRI control room.

Needle insertion experiments were performed using a prototype of the pneumatically-actuated tissue stabilization device in order to evaluate its effectiveness in stabilization of a target inside soft tissue; chicken breast tissue was used in the tests. A miniaturized electromagnetic sensor was inserted inside the tissue as the target to monitor the displacements. Electromagnetic position sensors were also attached to the needle and the support plates to track their movements. Different test procedures corresponding to the proposed control strategies were performed to evaluate the stabilization device performance. Another experiment was also carried out using a conventional parallel plates system configuration to compare the stabilization performance results. The proposed control strategies were proved to be effective in compensating for the target and the needle initial misalignment as well as target movement due to the needle insertion forces. The optimal shape support plates provide comparable tissue stabilization compared to that of parallel plates approach while applying significantly lower stress to the tissue. MR-compatibility tests revealed no significant image distortion while despite the moderate drop in signal to noise ratio (SNR), the values remained in an acceptable range for detecting a lesion in the MR image.

1.3 Thesis Organization

The rest of the thesis is organized as follows: Chapter 2 provides a literature review on the breast biopsy stabilization methods and MR-compatible robotic devices. It also covers the studies that define MR-compatibility design criteria of mechatronic devices. Chapter 3 discusses an overview of the proposed system for MRI-guided breast biopsy and elaborates on the device design requirements, while also discussing a study conducted by (Chen, 2013) to perform shape optimization of the tissue stabilization plates that offers major improvements over parallel plates configuration. Two concept designs for piezoelectric-based devices are also presented. Chapter 4 introduces an element-by-element model of the pneumatically-actuated mechanism as well as control strategies for biopsy target stabilization using the new device. Experimental and MR-compatibility test results are reported in Chapter 5. The thesis is concluded in Chapter 6 where some possible directions for future work are also discussed.

1.4 Related Publications

- Iranpanah, B., Chen, M., Patriciu, A., and Sirouspour, S. A Pneumatically Actuated Breast Stabilization Device for MRI-Guided Breast Biopsy. To be submitted to *IEEE/ASME Transactions on Mechatronics.*
- Patriciu, A., Chen, M., Iranpanah, B., and Sirouspour, S. A Tissue Stabilization Device for MRI-Guided Breast Biopsy. Submitted for publication to *Medical Engineering & Physics.*

Chapter 2

Literature Review

In this chapter, the existing literature in the area of MRI-guided breast biopsy is reviewed. The review will also cover some of the newer techniques that have been proposed to overcome the limitations associated with the conventional breast compression in parallel plates configuration. This review is not intended to be exhaustive but rather provides a proper context for work in this thesis. It will help us identify the shortcomings of the available techniques that need to be overcome by the new technology proposed in this research. It will also inform the design of the tissue stabilization device to ensure compatibility with current standard of practice and other system components.

2.1 Breast Cancer and Biopsy

Early detection of breast cancer in women in high risk of developing breast cancer is crucial. The importance of mammographic screening has been widely recognized over the years as routine semi-annual clinical breast examination is recommended (Kopans, 1992). However, it is often hard to definitely diagnose diagnosis of mammography-detected lesions (Kopans, 1992). Mammography screening has a low sensitivity in women with dense breast; roughly while half of the women population is classified as having dense breast tissue (Goldfischer, 2010). Histopathological examination is considered as the “Gold Standard” for definitive diagnosis. Tissue sample can be collected through needle biopsy or open surgical biopsy. There has been a steady decline in use of open surgical biopsy since needle biopsy is less traumatic, allows for quicker recovery, and offers comparable diagnosis accuracy (Mallapragada *et al.*, 2007).

Fine needle aspiration (FNA) is the most basic form of sampling that has been used for diagnosis since 1950s. The needle is attached to a plastic syringe to produce sufficient suction to obtain the sample. It is a simple technique that can be tolerated by the patient but due to the high rate of insufficient samples and reduced potential diagnostic yield of FNA with diffuse thickening in the breast, it is no longer considered as a routine technique.

Image-guided core biopsy (CB) became the clinical standard practice following Parker *et al.* (1993) publication. The biopsy gun consists of a spring-loaded automated needle that allows small cylinders of tissue to be cut and collected by the needle. Following the acquisition of each core sample, the needle needs to be removed to obtain the tissue and must be re-inserted for further samples that would severely damage the breast tissue. The optimal number of necessary specimens for a definitive diagnosis depends on the type of the suspicious lesion; however, diagnostic accuracy is improved by increasing the number of samples. False-negative (range 0-9%) results are another drawback of the core biopsy method that can be caused by inaccurate tissue sampling.

Currently, Vacuum-assisted biopsy (VAM) is the most commonplace biopsy method that addresses the limitations of CB. VAM is powered with suction and a rotating cutter, which obtains multiple samples from the lesion. The samples are collected in the specimen port and multiple samples can be acquired without removing the needle. Standard VAB is usually performed with a 10 or 11G (3.4 and 3.0 mm in diameters) needle. False-negative rates for vacuum-assisted biopsies are lower, ranging from 1.3 to 3.3% (O'Flynn *et al.*, 2010; Pijnappel *et al.*, 2004; Zuiani *et al.*, 2007).

Ultrasound is the preferred image modality to perform image-guided breast biopsy as it is quick, widely accessible, and less costly than the other modalities. Real-time ultrasound is the most convenient guidance method to obtain biopsy samples both for the patient and physician. FNA, CB, and VAB can all be performed under ultrasound guidance mainly for superficial lesions. Three-dimensional (3D) ultrasound has multiplanar display that follows the exact position of the needle during biopsy.

Stereotactic breast biopsies are performed to obtain lesion samples that are detected on mammography but cannot be visualized with ultrasound. Stereotactic-guidance procedure can be performed using standard upright mammography machines with the patient lied prone on a special table. The breast falls through a hole in the table is compressed between two parallel mammographic plates. Breast immobilization is crucial for the duration of the procedure (20-45 minutes) to ensure the patient in a stable position (O'Flynn *et al.*, 2010).

Contrast-enhanced MRI images provide additional information about the lesion with a precise determination of the extent of the disease. Most MRI-guided biopsies are performed in closed-bore MRI machines while the retrieval of specimens are carried-out outside the magnet. A stereotactic system including compression parallel plates, MRI imaging coil, and aiming device are used to immobilize the breast in place. The strong compression of breast in these procedures may degrade lesion enhancement and distort breast anatomical structure (Viehweg *et al.*, 2002).

2.2 MRI-Guided Breast Biopsy

Several researchers have investigated methods for dealing with tissue movement during soft-tissue biopsy. Graessle *et al.* (2007) have re-designed existing parallel gridded plates to address patient discomfort in the highly compressed parallel plates method. The new stabilization plate has a convex curvature and the biopsy needle is still inserted in the lateral direction, but the curvature in gridded paddles helps maintain the breast in a more natural form while applying less forces to the tissue. Kobayashi *et al.* (2012) investigated the effect of using pre-loading on minimizing target displacement during needle insertion. Their system includes a mechanical probe that presses the breast tissue to stiffen the area between the tumor and needle tip. They demonstrated the effectiveness of pre-loading force in minimizing target movements. Smith *et al.* (2008) developed a biopsy system that localizes the lesion in a radial coordinate system. The device consists of a 360 degrees rotating platform combined with solenoid imaging coils and a needle driver mechanism. The insertion entry point is selected on the side of the breast for minimal tissue penetration. The coil is equipped with three circumferential air bladders that will be inflated to immobilize the breast. An improved pressure distribution in comparison to the parallel plates approach allows the breast to remain in a more natural form while mitigating some of the pain experienced by the patient.

Azar *et al.* (2002) used a finite element model of the breast to predict target movement. In their approach, patient's MRI image data is used to construct a geometrical model of the breast and the mechanical properties are assigned according to a non-linear material deformation model. With this method, the breast can be pre-operatively imaged without or with a gentle compression force. The tissue can then be compressed during the procedure while the finite element model is employed to predict the target location. The full procedure can be performed in less than 30 minutes in a clinically useful amount of time. The geometrical model and mechanical properties of the breast are essential for accurate movement predictions. However, the complexity of breast tissue (anisotropy, inhomogeneity, the number and distribution of Cooper's ligaments) makes it difficult to accurately calculate breast tissue properties (Azar *et al.*, 2000). Other studies have also proposed finite element models of the breast based on MRI image data for target movement predictions (Sarkar *et al.*, 2007; Del Palomar *et al.*, 2008; Pathmanathan *et al.*, 2004).

In another approach, Okazawa *et al.* (2005) designed and implemented a steerable needle for percutaneous medical procedures. The needle driver is built by a slight modification to the stylet of a standard medical biopsy needle. The needle driver offers two degrees of steering freedom with the mechanical actuation of the stylet with respect to the needle cannula. Experimental results on tissue phantoms validated the effectiveness of steering performance, as a 30 mm of lateral tip motion was achieved in 100 mm insertion with a 20-gauge biopsy needle. The needle can be guided by the physician using a hand-held steering device, or can be controlled using a path-planning software package. However, needle steering inside the breast can damage healthy tissue. Webster III *et al.* (2005) have investigated design consideration for robotic needle steering by examining the influence of phantom and needle properties, bevel tip angle, needle insertion angle, and insertion speed on needle steering performance.

2.3 MRI-Guided Robotic Breast Biopsy

If properly employed, robots can improve the precision and outcome of many medical procedures. Several groups have proposed robotic devices to address the limitations of conventional MR-guided breast biopsy. Surgical robots usually require trajectory planning that is performed based on pre-operative images (Chinzei and Miller, 2000).

ROBITOM is a six degree-of-freedom (DOF) manipulator for biopsy and interventional therapy of of breast lesions. The system is designed to work inside the cylindrical space of a closed MRI scanner and is comprised of a plastic rack where two mounted piezoelectric motors drive an extension arm along two Cartesian directions. The probe at the end of the arm faces the patient and can be loaded with different instruments according to the desired application. The robot was placed in vicinity of a magnet, and experiments were carried out on pig livers, as targets with diameter of 4 mm were precisely hit by the robotic device (Kaiser *et al.*, 2000). Pfleiderer *et al.* (2003) successfully tested a prototype of ROBITOM in a clinical setting performing large core breast biopsy inside a 1.5 Tesla scanner. The device operated in the presence of high static magnetic field without any significant artifacts or distortions in the MR images. The first experiment revealed problem of lesion shifting and target missing. To address these complications, a second generation of the system, ROBITOM II, incorporated a high-speed trocar unit (Pfleiderer *et al.*, 2005). A dedicated double breast biopsy coil was also outfitted in the latest design to enhance imaging quality and access to the breast tissue. The system performed successfully during *in vitro* phantom and *in vivo* human tests inside a 1.5 Tesla scanner.

Larson *et al.* (2004) and Tsekos *et al.* (2001) developed a robotic device for breast biopsy and intervention under MR guidance. The apparatus is fitted with five DOF; four positional degrees of freedom are used to orient the probe while the fifth degree of freedom enables stabilization of the breast. With this design, the breast tissue is accessible from any desired orientations. This is achieved since two compression plates are mounted on a rotating base that determines the orientation of breast compression and thus the insertion axis. The device stabilizes the breast by compression and takes into account different breast conditions by adjusting orientation and the degree of compression. It is actuated by ultrasonic motors that are placed one meter away from the magnet bore during the experiments in a 4 Tesla scanner. However, excessive backlash in the rotational degrees of freedom resulted in significant positioning error; patient discomfort as a result of breast compression and limited maneuver options of the plates are some of the other drawbacks of this system.

Yang *et al.* (2011b) designed and implemented a pneumatically actuated MR-compatbile device with four DOF. The device consists of a parallel mechanism and a needle driver. The parallel mechanism provides three DOF to perform needle positioning while the fourth degree of freedom is used to drive the needle. The parallel mechanism is pneumatically actuated using long transmission lines and the needle driver is actuated with a piezo-electric motor. They achieved satisfactory positioning performance using this device and a sliding mode controller, but noted significant drop in the signal to noise ratio (SNR) of the MR images during the robot operation.

MDA Space Missions (Brampton, Ontario, Canada) and the Center for Surgical Invention and Innovation designed an in-bore robot for MR-guided breast biopsy

(ANVARI *et al.*, 2011). Their system is based on a superior-inferior approach for needle insertion as opposed to the lateral approach in the conventional parallel plates manual biopsy. In their system, the imaging coils can be placed close to the breast tissue as they have to be parallel to sagittal plane to achieve highest signal to noise ratio.

2.4 MRI-Compatible Robotic Devices for Other Applications

Several MRI-compatible robots have been developed for applications other than breast biopsy (Tsekos *et al.*, 2007). Masamune *et al.* (1995) who developed a six DOF MR-compatible manipulator for neurological stereotactic needle biopsies. Their study contributed to the first insights into challenges affiliated with MR-compatible devices. Assessment of the system in MR-guided targeting on phantoms revealed positioning error of 3 mm; however, the ultrasonic motors in this system significantly deteriorated the image quality and therefore needed to be turned off during MR scanning.

A general-purpose robotic system for MR-guided interventions was presented by Tsekos *et al.* (2005) and then further enhanced by Christoforou *et al.* (2007). The system consists of a three DOF Cartesian positioner located in front of the scanner, and a robotic arm that has three rotational DOF and a linear one for insertion of an interventional tool. Actuators are placed outside of the scanner at the end of arm while motion is transferred using drive shafts and universal joints. MR-compatibility studies demonstrated that enclosing of the electronics inside a Farady cage and shielding of the wires can substantially reduce noise due to the ultrasonic motors. *In vivo* studies on animals showed sufficient signal to noise ratio when the robot was in motion.

MIRA (Manipulator for Interventional Radiology) is a tele-robotic device for MR-guided therapies and operations (Hempel *et al.*, 2003). The system consists of three functional units; a positioning unit (arm structure, actuators, and position sensors), invasive components such as application modules for therapy, and a control unit that provides necessary tools for preparation and operation of the robot. Ultrasonic motors are employed to actuate the robot while a pneumatically actuated needle driver system is integrated for gripping and insertion of the needle close to the magnet bore. The system achieved a positioning accuracy of 1 mm in phantom tests and caused no significant artifacts in MR images when the robot was placed one meter away from the magnet.

MrBot is a fully actuated pneumatic robot for prostate interventions such as biopsy, thermal ablation, and brachytherapy (Stoianovici *et al.*, 2007a). The robot is multi-imager compatible capable of performing inside the scanner alongside the patient. A 5 DOF parallel link structure provides the required movements for positioning of the probe. Imager compatibility tests revealed no major artifacts in images. Patriciu *et al.* (2007) successfully tested the robot in brachytherapy seed placement *in vitro* experiments achieving an accuracy of 1.2 mm.

In another study, an MR-compatible robotic device for prostate therapeutic procedures was reported by Susil *et al.* (2004) and further improved by Krieger *et al.* (2005). A prototype of the system was tested performing *in vivo* prostate interventions with no adverse patient outcome. The device is one of the few that have been tested on humans in a closed-bore scanner.

NeuroArm is a MR-compatible robot designed to soft tissue manipulation, needle insertion, tissue grasping, and suturing. The system, developed in a collaboration between University of Calgary and MDA Space Missions (Brampton, Ontario, Canada), is comprised of two robotic arms, each with 6 degrees of motion freedom, and a third arm equipped with two cameras providing 3-D stereoscopic views. The robot end-effector is equipped with a unique tool actuation mechanism and 3 three-axis optical force sensors to provide haptic force feedback to the surgeon. It allows MRI feedback in all stages of operation without moving the patient. NeuroArm was the first robotic system to operate on a human patient in an image-guided neurosurgery to remove a brain tumor (Sutherland *et al.*, 2003; Bogue, 2011).

InnoMotion ^{TM}(Innomedic GmbH, Herxheim, Germany) is the only commercially available MR-compatible robotic system. It has a 6 DOF robotic arm capable of assisting in variety of applications such as pain therapy, tumor therapy, and biopsies. Specially designed pneumatic actuators are employed in the system for full MR-compatibility. The system was tested in an animal study for image-guided targeting in a 1.5 Tesla scanner (Bock *et al.*, 2005).

2.5 Design Criteria for MR-Compatible Devices

MR-compatibility requires a mechatronic device to be able to operate in the very strong field of the MRI magnet and at the same time cause no significant interference with imaging. To attain this designation, strict component design and material selection guidelines must be followed (Chinzei *et al.*, 1999). For a device to be MR-compatible:

- it must safely operate inside the MRI magnet.

- its operation inside the MR environment should not deteriorate image quality.
- MR environment should not affect the device functionality.

Additionally, location and timing *zones* are defined such that MR-compatibility of a device with respect to each zone should be declared.

Zone 1: device may operate inside the imaging region of interest during imaging and surgical interventions.

Zone 2: device may operate in imaging region during imaging and surgical interventions, but it is not in the region of interest.

Zone 3: device may operate in imaging region but removed during the image acquisition.

Zone 4: device may operate in the magnet room during surgical interventions but kept in a distance more than 1 meter from the magnet.

The strong magnetic field of MRI exerts high forces on ferromagnetic materials, which can cause a highly hazardous operating condition (Schenck, 1998, 2000; Shellock and Crues, 2004). Additionally, ferromagnetic martials can disrupt the homogeneity of the main magnetic field and can introduce susceptibility artifacts in MR images. The gradient of magnetic field can induce eddy currents in conductive materials, which would severely degrade image quality. The applied RF pulses and the magnetic field gradients of MRI can heat conductive interventional tools such as needles (Shellock and Crues, 2004; Moscatel *et al.*, 1995; Shellock and Shellock, 1998; Shellock, 2000; Keeler *et al.*, 1998).

Nonmagnetic and nonconductive materials such as plastic, ceramic, fiberglass, carbon fiber, and other composites are suitable for development of MR-compatible devices. However, their inadequate structural stiffness can have a negative effect on functionality of a mechatronic device. Small metallic parts have been employed in MR-compatible structures (Kaiser *et al.*, 2000). Small sized metallic parts, if placed appropriately relative to the imaging area, do not cause significant problems or image artifacts.

MR-compatible robotic systems require a suitable form of actuation. Manual actuation is the simplest form of actuation that is employed in a number of interventional devices designed to assist in prostate procedures (Krieger *et al.*, 2005). Elhawary *et al.* (2006) reviewed the compatibility and performance of four groups of actuators for operations inside MRI, namely ultrasonic, hydraulics, pneumatic, and remote manual actuation. Hydraulics actuation can be used with proper hydraulic fluid and components; for example, a hydraulically actuated six degrees of freedom manipulator for minimally invasive liver surgery performed inside open MRI scanner in (Kim *et al.*, 2002). The main problem with this form of actuation is fluid leakages and entrance of air bubbles into the pressurized system.

Piezoelectric actuators are commonly used in MR-compatible devices as their performance are not affected by strong magnetic field of MRI machine. Piezoelectric phenomenon causes a piezoelectric ceramic to vibrate when an electrical field is applied. This is translated to linear or rotary motion in piezoelectric actuators. Piezoelectric motors offer bidirectional movement, high torque to weight ratio, compact size, and high breaking force. This last feature could be a drawback where back-drivability is desirable, i.e. in the case of medical emergency or failure. Moreover, high frequency currents in these motors cause image distortion, if they are placed near the imaging coil (Hempel *et al.*, 2003).

Pneumatic actuators can safely operate in magnetic field and are cleaner and faster than their hydraulic counterparts. However, some of the limitations of these actuation method such as accuracy, limited stiffness, and patient safety need to be properly addressed for use in medical applications (Choi *et al.*, 2005; Elhawary *et al.*, 2006). PneuStep (Stoianovici *et al.*, 2007b) is a MR compatible pneumatic step motor designed for precise motion in a safe and controllable manner. PneuStep works based on a stepper motor principle to achieve precise motion control in the order of 0.050 mm, making it suitable for actuating image-guided interventional robots. The motor has been integrated into a commercial robotic system, InnoMotion $^{\text{TM}}$, and has been successfully tested in a 7 Tesla scanner without any image artifacts and loss of motion accuracy.

Sensor selection is another important aspect of the design of an MR-compatible system. Custom designed incremental encoders for translational and rotational measurements have been proposed. They commonly use glass grating pattern for measurements and fiber-optic cables to transfer signals to a remote location where an optical component and circuitry is placed (Chinzei *et al.*, 2000). Takahashi *et al.* (2003) developed a six-axis force sensor for MRI applications; using fiber-optic components, a similar sensor was employed in a MRI-compatible haptic device for applications such as assistive devices for interventional MRI and haptic interfaces for neuroscience investigation (Gassert *et al.*, 2006). In these cases, a fiber cable transmitted the light to a remotely placed other part of the sensor and the signal was continued through a returning cable. Physical displacement of the sensing element due to the applied force alters the passage of light between the two cables was measured to derive the size of the force. Tada and Kanade (2004) presented and tested a force sensor based on optical micrometry. Load cells have also been used in MR environment (Khanicheh *et al.*, 2005; Cramer *et al.*, 2002). These sensors are made of conductive materials such as aluminium, and require a small size that need to be placed properly relative to the imaged area. They convert deformation strain to electrical signals.

Chapter 3

Design and Implementation of the Stabilization Device

In this chapter, first a system level concept overview of the proposed system for MRI-guided breast biopsy is presented. Then, the systematic approach for optimization of the support plates geometry in the tissue stabilization device from the work by Chen (2013) is briefly reviewed. This is followed by a discussion of design requirements for the pneumatically-actuated tissue stabilization device. Finally, conceptual design for a piezoelectric-actuated needle driver as well as a tissue stabilization device are presented.

3.1 System Concept Overview

A CAD model of the proposed system for MRI-guided breast biopsy is given in Fig. 3.1. The system is comprised of a pneumatically-actuated breast stabilization device, a needle driver mechanism with two active translational DOF along the y and

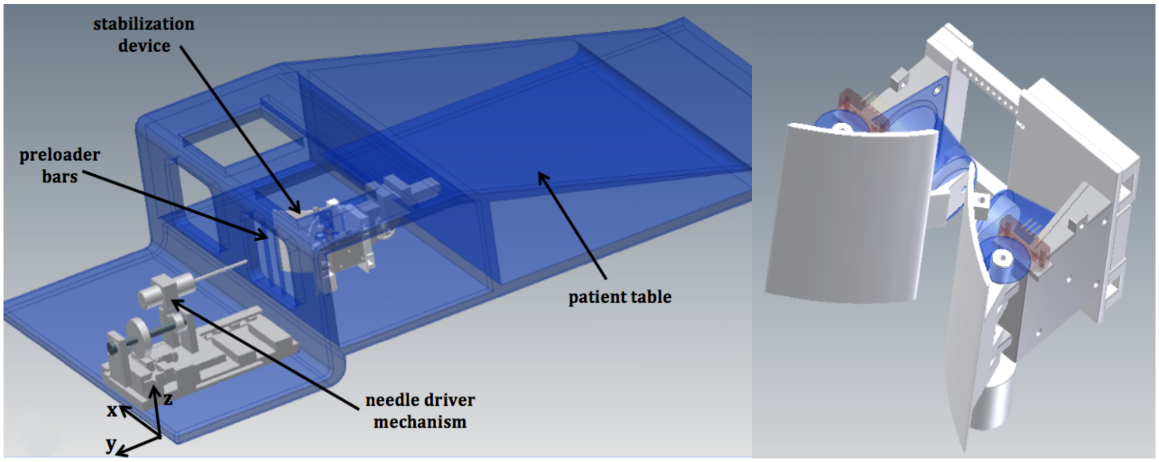

(a) (b)

Figure 3.1: a) CAD model of the proposed system for MRI-guided breast biopsy. b) Breast stabilization device with two pneumatically-actuated tissue support plates.

z axes, and a patient table. Alternatively, the pneumatic device could be replaced by a piezoelectric device. In the pneumatic tissue stabilization device, the lateral position of the support plates of the stabilization device can be manually positioned along the x axis whereas their orientations are actively controlled by pneumatic actuators. In the device actuated by piezoelectric motors, the lateral motion is also actuated. The translation DOF of the needle drive mechanism are equipped with piezoelectric actuators. The main focus of this thesis is on the design and evaluation of the pneumatic breast stabilization component of the system in Fig. 3.1.b. However, concept designs for the needle driver and a piezoelectric version of the tissue stabilization device have also been developed and will be reported.

With this system during the biopsy procedure, the patient would lie prone on the table and the support plates of the stabilization device would be manually positioned in the mideo-lateral direction (along the x axis) to encompass the breast and roughly align the biopsy target with the needle insertion path. It is assumed that the quadrant of the breast in which the biopsy target lies would be known from a diagnostic image. The support plates would push the breast against two pre-loader bars, embedded at the front opening of the table, in the y direction to help hold the breast firmly in place; this is also done manually. Next, the patient would be moved into the MRI scanner to acquire pre-operative MR images, which would be used to localize the biopsy target. Once the target location is determined, the angles of the two support plates and the elevation of the needle in the z-direction could be adjusted without removing the patient from the imager in order to precisely align the biopsy target with the needle insertion path. The needle is then driven inside the the tissue along the y-axis to reach the target. Further changes to the plate configuration, needle elevation, and needle insertion depth could be made based on feedback from subsequent intra-operative MR images, if available.

3.2 Shape Optimization of Stabilization Plate

The breast stabilization mechanism in Fig.3.1.b consists of two actively-controlled support plates that would stabilize the biopsy target mainly through the geometry of the plates, and small in-magnet movements of the plates if and when needed. One of the objectives of this approach is to reduce the patient pain and discomfort associated with high compression forces in the conventional parallel-plates/grids systems and at the same time provide comparable tissue stabilization. Furthermore, the open-access configuration of the proposed breast stabilization device offers more freedom in the selection of needle insertion entry point and insertion path compared to the parallel gridded plates. The two support plates are connected by a flexible mesh; the breast tissue is positioned between the plates while the two preloaded bars restrain it in place. With this configuration, the needle is inserted in a superior-inferior direction using a separate needle drive mechanism.

The shape of the support plates can significantly impact how well target movements are stabilized during biopsy. A systematic approach for optimization of the plates geometry has been recently developed in our group and is reported in Patriciu *et al.* (2013) ; this approach is briefly reviewed here. To facilitate the formulation of the optimization problem, the plate geometry is parametrized by a finite set of variables using a cubic Bézier function (Haslinger and Mäkinen, 2003):

$$B(t) = (1-t)^3\alpha_0 + 3(1-t)^2 t\alpha_1 + 3(1-t)t^2\alpha_2 + t^3\alpha_3 \tag{3.1}$$

where $t \in [0,1]$ and the control points $\alpha_0, \alpha_1, \alpha_2, \alpha_3 \in \mathbb{R}^2$ are the design parameters shown in Fig. 3.2.

The optimization problem is formulated as a minimization of the maximum target displacement inside a region of interest over the space of the design parameters. Only biopsy scenarios involving targets in a deep region of breast are considered since ultrasound-guided biopsy can be effective for superficial lesions. The plate optimization problem is formally formulated as

$$\begin{aligned} (\alpha_1^m, \alpha_2^m, \alpha_3^m) &= \mathrm{argmin}_{\alpha_1,\alpha_2,\alpha_3\in\mathbb{R}^2} \left(\max\nolimits_{T\in\Omega_T} \Delta d(T)\right) \\ &\text{s.t. } \alpha_1, \alpha_2 \in [30,60]\times(0,110) \\ &\quad 0 < \alpha_{1y} < \alpha_{2y} < \alpha_{3y} < 110 \end{aligned} \tag{3.2}$$

where $\Delta d(T)$, a function of design parameters α_1, α_2, α_3, is target displacement for a desired needle tip position T. A 2-D computational deformation model is employed for the calculation of the cost function; the breast is considered to be homogeneous, isotropic and with incompressible fat tissue (Azar *et al.*, 2000).

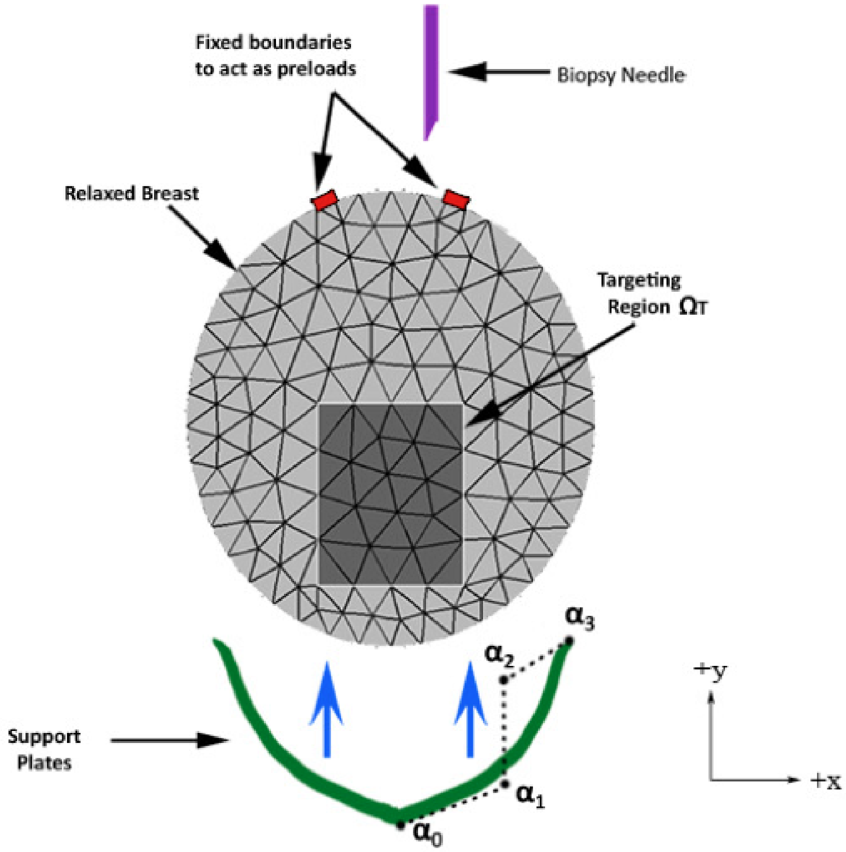

Figure 3.2: The support plates in the breast stabilization device with a model of the breast tissue used for plate shape optimization; the plate shape parameters are $\alpha_1 - \alpha_3$.

A derivative-free direct search method, known as the surrogate management framework (Booker *et al.*, 1999), was employed to solve the optimization problem in (3.2). Optimal values for the control parameters of the plate geometry are given in Table 3.1.

A prototype of the mechanism without the pneumatic actuators was first built in order to validate the effectiveness of a passive breast stabilization device that merely relies on the support plates geometry to minimize target displacements.

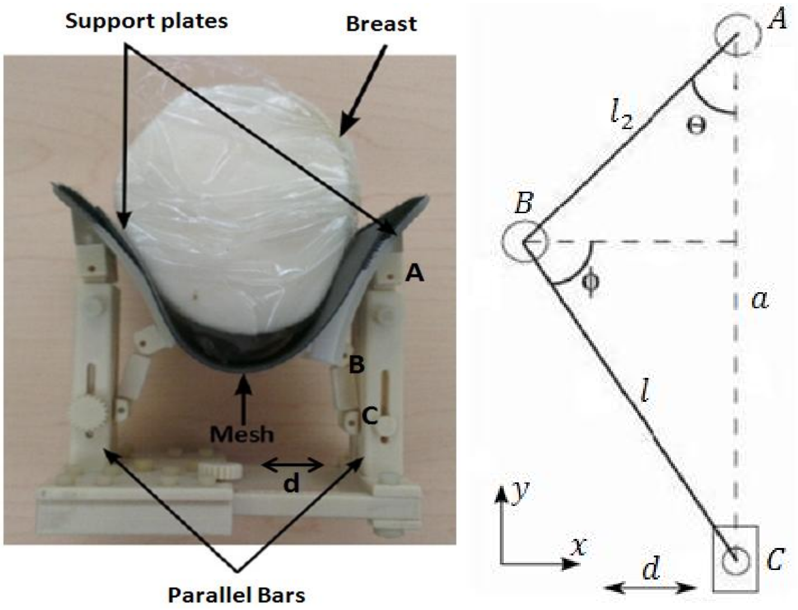

(a) (b)

Figure 3.3: a) The passive stabilization plate. b) Simplified schematic of the adjusting mechanism.

3.2.1 Passive Stabilization Device

Fig. 3.3a shows the passive stabilization device. The support plates can rotate around axis A while the lateral distance of the plates can be adjusted using the lateral slider d. Slider position is selected from a finite set of discrete positions using a pin and hole locking mechanism. A simplified schematic of the adjustment mechanism, a crank and slider, is shown in Fig. 3.3b with AB link being the crank and C resembling the slider. At the same time, all mechanism components are mounted on a lateral slider that moves along the x direction.

Assuming an end-effector point in the middle of link l_2, the relation between the end-effector forces expressed in the reference coordinate system (F_{ext}), and the forces of the prismatic joints (F_d ,F_a) can be expressed as

$$\begin{bmatrix} F_d \\ \\ F_a \end{bmatrix} = \underbrace{\begin{bmatrix} 1 & -\frac{(l_2 cos\theta - a)}{2a\tan\theta} \\ \\ 0 & \frac{(l_2 cos\theta - a)}{2a} \end{bmatrix}^T}_{J^T} \begin{bmatrix} F^x_{ext} \\ \\ F^y_{ext} \end{bmatrix} \tag{3.3}$$

with J being the Jacobian matrix relating the end-effector velocities $\begin{bmatrix} \dot{x} & \dot{y} \end{bmatrix}$ to the joint velocities $\begin{bmatrix} \dot{d} & \dot{a} \end{bmatrix}$. A simple analysis can be carried out to calculate maximum joint forces required from the mechanism. To this end, it is assumed that the tissue interaction forces are concentrated at the midpoints of the plates. The maximum joint forces resulting from the application of a force of $5N$ overall possible directions in the range of 0-180 degrees (see the frame in Fig. 3.3b) all possible joint configurations is 5N and 8N in the lateral (d) and superior-inferior (a) directions, respectively. This force analysis was used to calculate the safety factor for the embedded locking pins.

3.2.2 Needle Insertion Experiments

To verify the effectiveness of the design, a prototype of the passive tissue stabilization with the optimal plate shape was developed and used to perform needle insertion tests. Two other non-optimal plate shapes (flat plates and outward curving plates) shown in Fig. 3.4 were also tested to evaluate the effect of optimal plate shape on target stabilization. Furthermore, needle insertions were also performed using parallel plates approach for comparison.

Needle insertions were performed on chilled chicken breast tissue, similar to Smith *et al.* (2008), using electromagnetic position sensors as targets. Three different plate

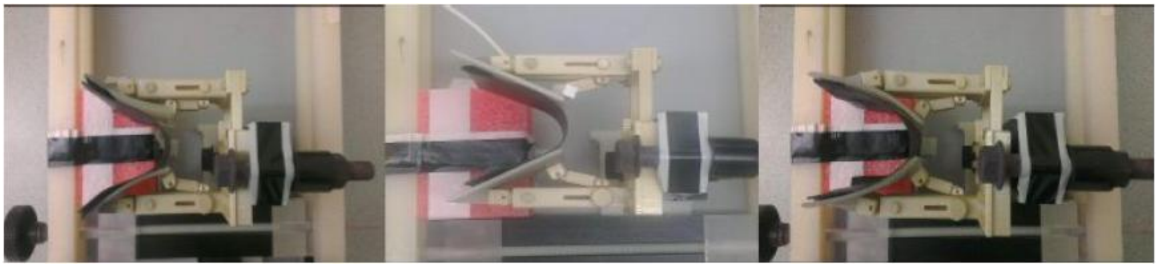

Figure 3.4: Plate designs used in the needle insertion experiments. From left to right respectively: optimal plate shape, flat plates, and convex plate shape.

geometries were compared in the experiments : i) the optimal plate shape ii) a flat plate shape, and iii) a suboptimal plate geometry. The compliance, defined as ratio of the target displacement to the insertion force, was calculated to normalize target displacement by the insertion force across all experiments. The results of these experiments are summarized in Table 3.2.

Table 3.1: Optimal α values for the support plate geometry

	α_0	α_1	α_2	α_3
x	0	30	30	65
y	0	15	55	90

Table 3.2: Experiment Results

	Optimal Shape	Flat Plates	Outward Curving Plates
Mean Total Displacement [mm]	1.8	2.3	2.7
Mean Target Compliance [mm/N]	0.57	0.56	0.66

The proposed device with the optimized plate shape yields comparable target stabilization to those recorded for a parallel plates configuration with a significant

53% compression, i.e. see Table 3.3. Moreover needle insertion forces are significantly lower in the proposed breast stabilization device with optimal plate geometry.

Table 3.3: Experimental results of optimal shape and parallel plate configuration

	Mean Target Displacement $[mm]$	Max Target Displacement $[mm]$
Parallel Plates 53% Compression	3.3	4.7
Optimal Shape	1.8	4.2

Our first prototype of the breast stabilization device reported in Patriciu *et al.* (2013) is a passive system with the optimized plate geometry. Building upon this concept, in the rest of this thesis two actuated variations of the device are presented that offer a couple of key advantages over the passive design. The passive device requires manual adjustments to the plate configuration by the physician outside the magnet to ensure proper alignment of the biopsy target with the needle insertion path since the physician access to the patient is extremely limited inside the magnet. This could prolong the procedure because of the time needed to move the patient in and out of the machine to make the adjustments. Moreover, no further changes to the plate configuration are possible after the start of the needle insertion phase. With an actuation mechanism that can operate inside an MRI magnet, plate adjustments can be carried out with the patient inside the machine, significantly reducing procedure time and possibly improving targeting accuracy. In addition, as real-time/fast MR imaging is becoming a reality, on-the-fly plate configuration adjustments can be made to further compensate for any possible targeting errors due to tissue deformation, patient movement, or registration inaccuracies.

3.3 Pneumatically-Actuated Tissue Stabilization Device

MR compatibility is one of the main constraints in the design of the actuated breast tissue stabilization device. The materials used to build the device must be nonmagnetic for safe operation. Electromagnetic interferences with the MR imaging that cause noise and image artifacts are also of significant concern. Ferromagnetic materials are commonly employed to construct mechatronic devices, because of their favorable mechanical properties, such as strength, rigidity, and machinability; however they are incompatible with MRI for obvious reasons. Instead, plastic, ceramic, and fiberglass have been widely used in the construction of MR-compatible devices (Tsekos *et al.*, 2007). Electric motors, which are commonly used for actuation in mechatronics devices, are also clearly unsuitable for operating inside MRI machines. Moreover, the limited space under the patient bed between the reception coils imposes a tight constraint on the size of the mechanism. This must be carefully considered in the design while trying to achieve sufficient plate movements for making in-bore adjustments.

All parts of the device are prototyped by a 3-D printer (ProJet™HD 3000) out of VisiJet®EX200, a plastic material used for 3-D modeling. Plastic parts minimize undesirable effects on MR magnetic field homogeneity and image artifacts. Furthermore, glass-filled nylon screws are used as fasteners in the device assembly. The only non-plastic parts used in the device are two incremental optical encoders (US Digital EM1-1-200-I, 1 inch inside diameter and 200 counts per revolution) for measuring the plate angles.

The first design of the active tissue stabilization device is based on the pneumatic

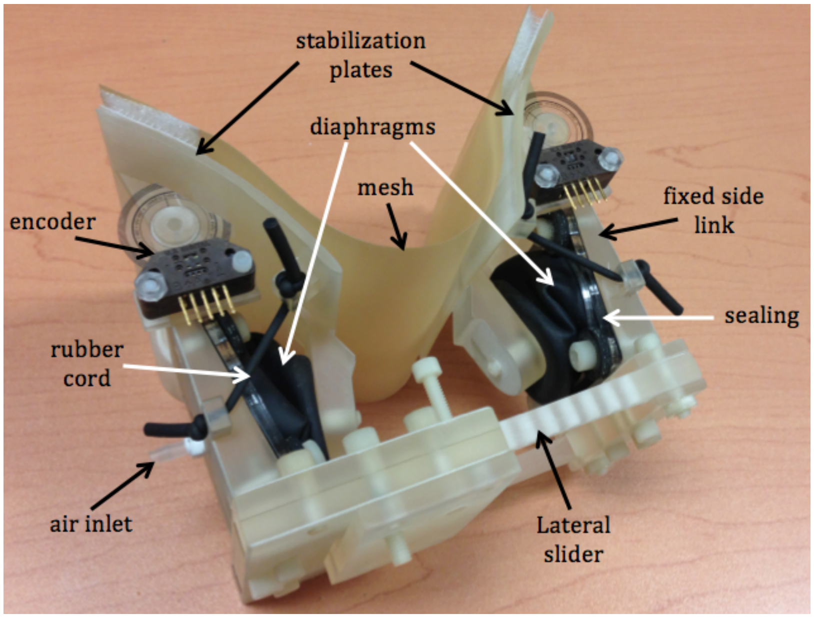

Figure 3.5: Prototype of the active tissue stabilization device with pneumatic actuators.

actuation using inflatable diaphragms. The pneumatic actuators can safely operate inside MRI and can be prototyped at a low cost.

A picture of the prototype breast stabilization device is shown in Fig. 3.5. The device is actuated via inflatable diaphragms (Diacom Corporation F-156-141, 1.56 inch cylinder diameter, 1.38 inch piston diameter). The diaphragms are mounted on the surface of the fixed side links and are properly sealed. When inflated through air inlets on the fixed side links, they generate torque to rotate each plate around the corresponding axis A, i.e. see Fig. 3.6. The air is supplied through long transmission lines by pressure-controlled valves; these are placed outside the MRI room. A rubber cord connects each plate to the fixed side link to apply reversing torque to the plates. The relative distance of the support plates can be adjusted manually to accommodate different breast sizes by sliding the right side of the mechanism in and out of the

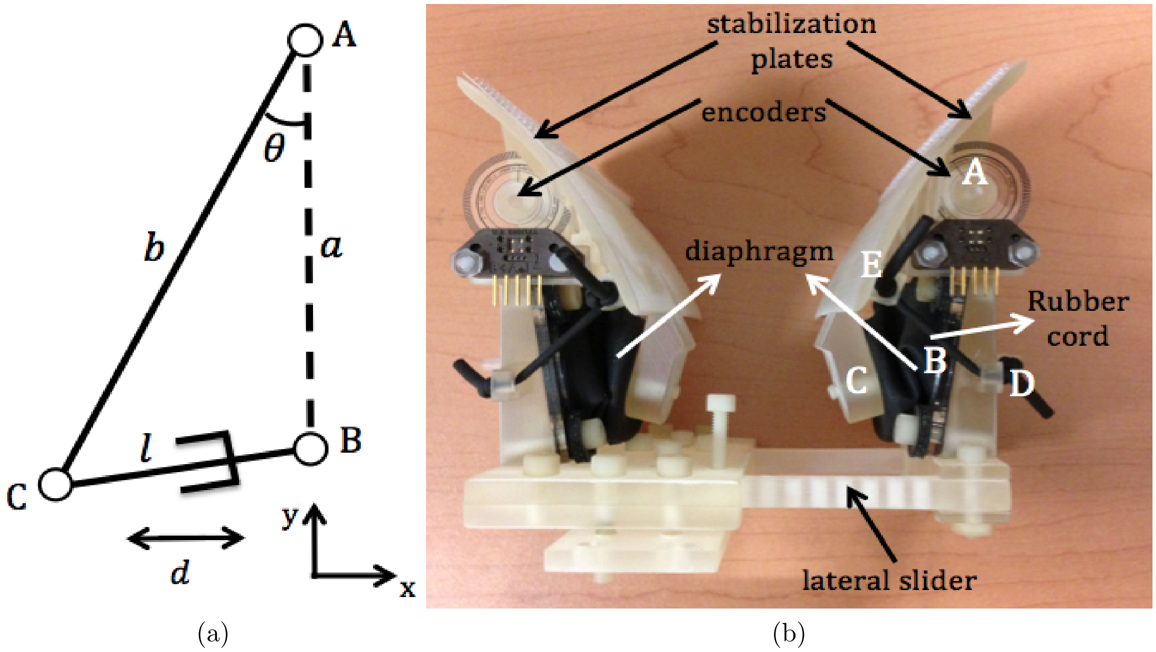

(a) (b)

Figure 3.6: a) Simplified schematic of the mechanism. b) A top view of the prototype.

device base. The plates can be positioned in fixed relative distances using a screw and hole locking mechanism. A few extreme configurations of the breast stabilization device in its workspace and the corresponding values of plate angles and distances are illustrated in Fig. 3.7. A detailed analysis of the device and its model are presented in Chapter 4.

3.4 Needle Driver Mechanism Concept Design

A concept design for a needle driver system using piezoelectric actuators (Nanomotion-HR4) and custom-made linear bearings has been developed. Piezoelectric actuators operate based on the piezoelectric effect that is understood as linear electromechanical interaction between the mechanical and the electrical state in crystalline materials.

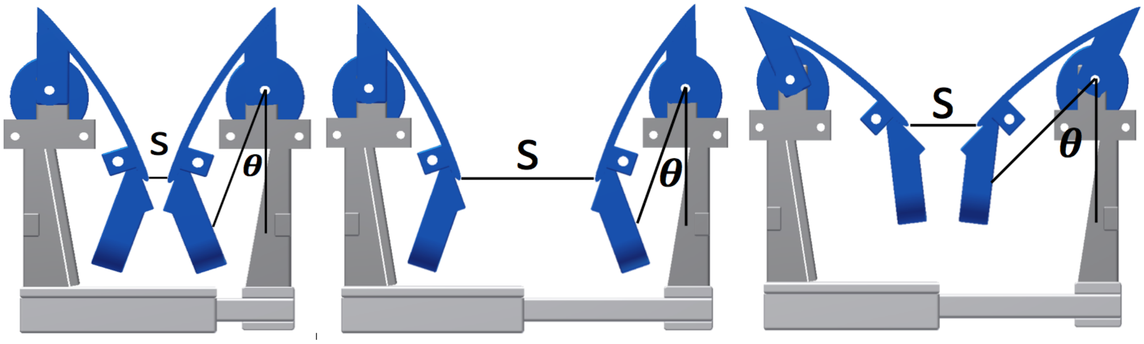

(a) (b) (c)

Figure 3.7: A few extreme configurations of the breast stabilization device with the corresponding rotation and relative distances of the support plates. a) $\theta = 18°$, $s = 5mm$. b) $\theta = 18°$, $s = 45mm$. c) $\theta = 40°$, $s = 25mm$. Note that only symmetric configurations are demonstrated here, but asymmetric configurations are also possible.

The piezoelectric effect causes internal generation of electrical charge resulting from applied mechanical force. This effect is reversible as the material exhibits the reverse piezoelectric effect with internal generation of mechanical strain resulting from applied electrical field. Piezoelectric actuator takes advantage of piezoceramics. Under special electrical excitation, longitudinal extension and transverse bending oscillation modes are induced at close frequencies (Krautkrämer and Krautkrämer, 1990). The simultaneous excitation of the longitudinal extension mode and the transverse bending mode creates a small elliptical trajectory of the ceramic edge. By coupling the ceramic edge to a precision stage, a driving force is exerted on the stage causing its movement. The driving force is applied periodically at frequencies much higher than the mechanical resonance of the stage, allowing continuous smooth motion for unlimited travel, while maintaining high resolution and positioning accuracy.

Linear piezoelectric actuator is usually coupled with a ceramic strip under a preloading force. The ceramic strip must be mounted on a kinematic rail system with

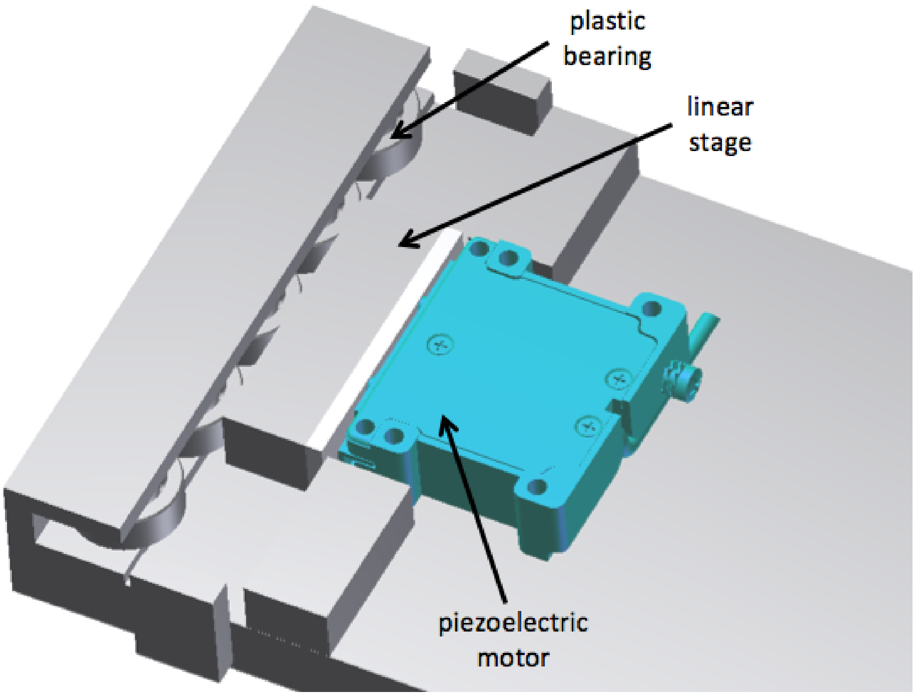

Figure 3.8: Custom designed linear bearing.

equipped linear bearings to reduce the friction along the motion axis.

CAD drawing for the proposed linear bearing mechanism is shown in Fig. 3.8. The moving stage is in contact with the actuator legs on one side, and plastic linear bearings on the other side. Linear bearings allow the stage to slide frictionless while providing the required preloading force (pushing and pulling of the stage is based on friction) between the stage and actuator legs. The stage movement is restricted in other directions. A prototype of the linear bearing was built and tested. Fig. 3.9 shows the prototype of the linear bearing using a Nanomotion HR4 piezoelectric actuator and its driver amplifier (Nanomotion AB1A Driver Amplifier). In this prototype, a simple fixed stage supports the linear stage and provides the required pre-loading force between the ceramic strip and piezoelectric actuator legs. HR4 actuators can provide a maximum velocity of $250mm/sec$ and a dynamic stall force of 15 to $18N$.

During the experiments it was discovered that, due to the friction between the linear and fixed stages, the actuator had to overcome a static friction force of close to $9N$ to drive the linear stage. This would reduce the linear stage output force and maximum velocity. Replacing the fixed stage in this prototype with an array of plastic ball bearings (shown in Fig. 3.8) will significantly reduce the friction force and improve the actuator performance.

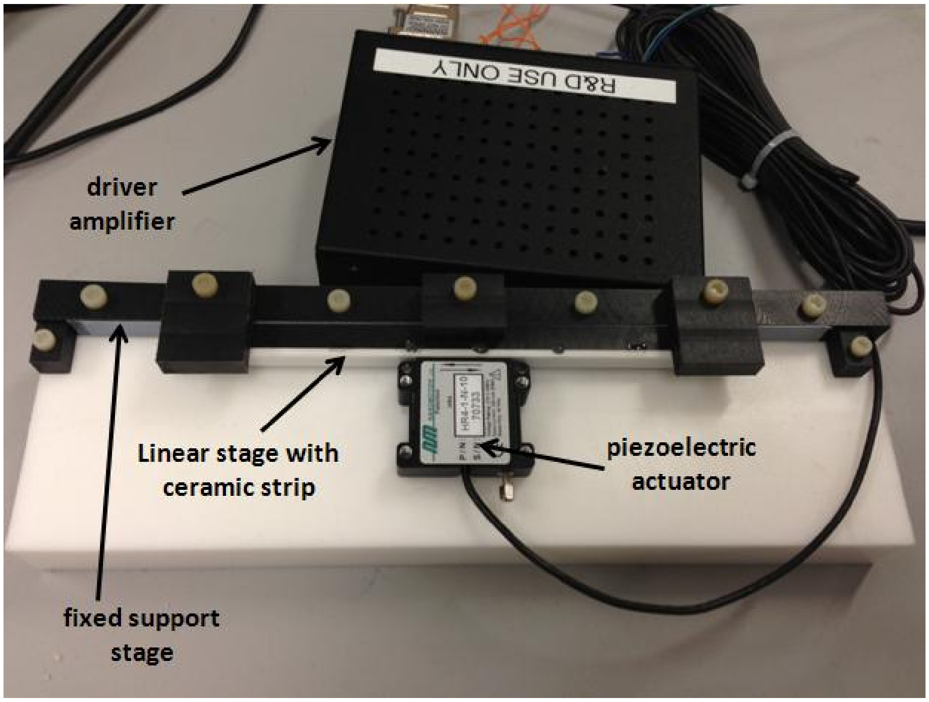

Figure 3.9: A test prototype of the custom-made linear bearing.

A needle driver mechanism with two DOF shown in Fig. 3.10, is designed using the linear bearings. The first linear stage drives the moving stage and therefore, the biopsy needle. This degree of freedom performs the needle insertion along its 130 mm travel range. The linear movement of the second stage is transferred to the elevation adjustment stage using a rack and pinion mechanism. This allows for elevation adjustment of the biopsy needle in a 45mm range. The static stall force for the elevation adjustment mechanism is significantly higher that the actuator stall force due to the employed gear reduction rate. The elevation adjustment mechanism is mounted on the first linear stage.

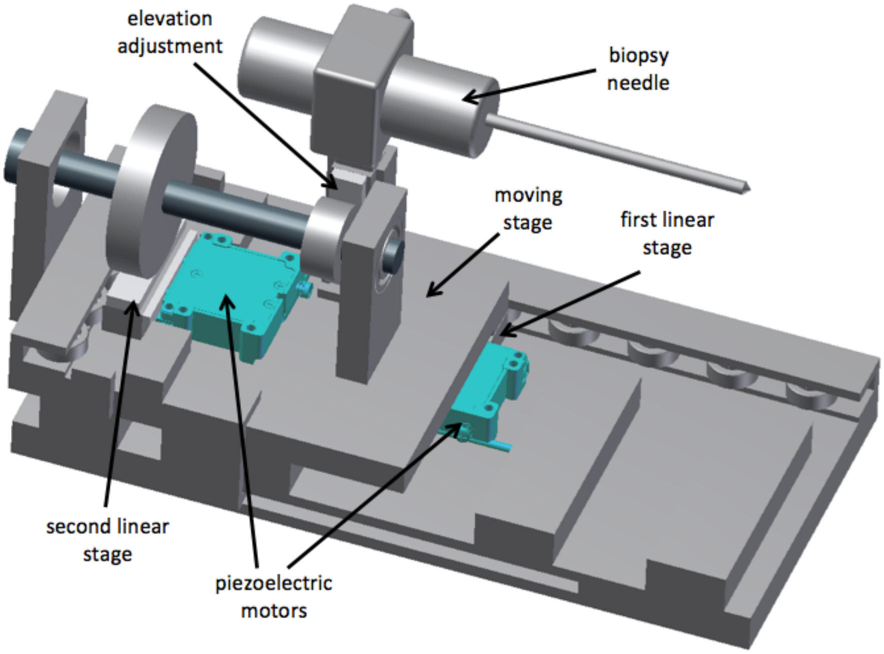

Figure 3.10: Needle driver mechanism concept design.

3.5 Three DOF Tissue Stabilization Device Concept Design

Using the custom-made linear bearings, a concept design for a tissue stabilization device with three degrees of freedom has been developed. Fig. 3.11 shows an overview of plate adjustment mechanism in this design. Orientation adjustment of each plate is achieved by movement of the superior-inferior slider along y axis that causes the plate to rotate around axis A. The lateral slider movement adjusts the lateral distance of the stabilization plates as the third degree-of-freedom of the plates.

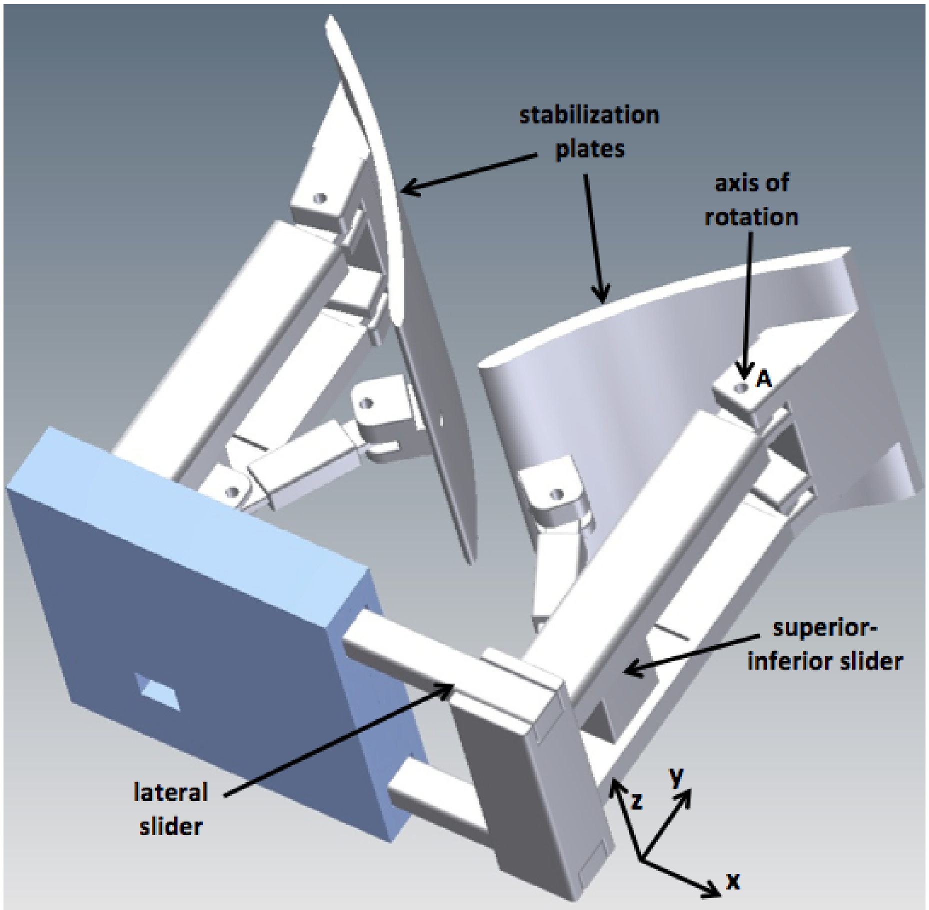

Figure 3.11: The stabilization device with three DOF.

Two superior-inferior sliders and the lateral slider are driven using piezoelectric actuators (Nanomotion-HR2). Fig. 3.12 shows the configuration of the three actuators in the device. The linear motion of the superior-inferior actuators is transferred to the superior-inferior sliders while the lateral actuator (Nanomotion-HR4) mobile stage is directly connected to the lateral slider. The locking mechanism of the sliders is based on the static stall force of the actuators (7N for HR2 and 1N for HR4). The base of the adjustment mechanism is similar to that of the passive tissue stabilization device described in Section 3.2.1. A kinematic force analysis revealed maximum forces of $5N$ and $8N$ in the lateral and superior-inferior slider, respectively. These forces are within the operation range of the HR2 (7 to $9N$ dynamic stall force) and HR4 actuators (15 to$18N$ dynamic stall force). The device provides 25 degrees of rotation range for each support plate as well as a $60mm$ lateral slider travel range. A prototype of this two DOF stabilization device is under development and will be reported in a future publication.

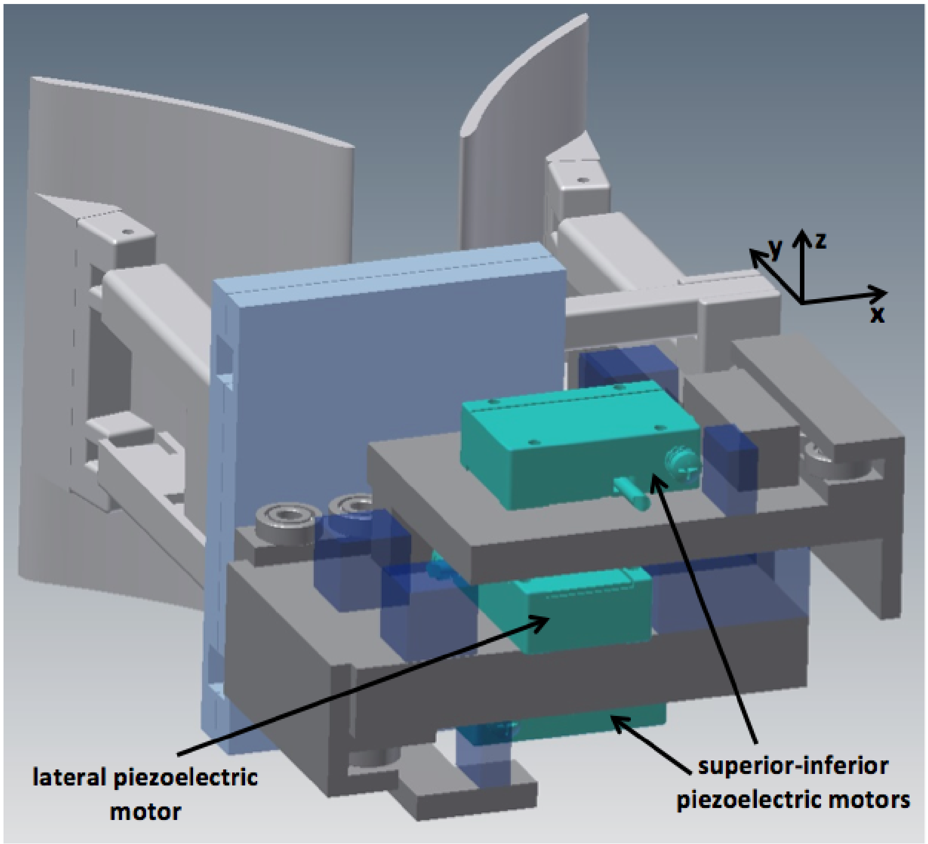

Figure 3.12: Configuration of the piezoelectric actuators in the concept design of a three DOF tissue stabilization device.

Chapter 4

Modeling and Control of Pneumatic Tissue Stabilization Device

In this chapter, a kinematic force analysis of the proposed pneumatically-actuated tissue stabilization device is performed. Models for different components of the device are also presented. A two-layer controller structure and two control strategies are then proposed to actively adjust the stabilization plates configuration according to MR feedback in order to overcome the target and needle misalignments. A frequency response analysis of the closed-loop control system is also performed.

4.1 Force Analysis

A simplified schematic of the mechanism is shown in Fig. 3.6.a. In this figure, link AC represents the support plate and the prismatic joint on link BC models the inflatable diaphragm between the fixed stage (AB) and point C. The whole mechanism can slide laterally (slider d) along the x direction. Assuming an end-effector point in the middle of link AB, the relation between the end-effector forces expressed in the reference coordinate system (F_{ext}), and the forces of the prismatic joints (F_d ,F_l) can be expressed as

$$\begin{bmatrix} F_d \\ \\ F_l \end{bmatrix} = \underbrace{\begin{bmatrix} 1 & -\frac{\sqrt{a^2+b^2-2ab\cos\theta}}{2a\tan\theta} \\ \\ 0 & \frac{\sqrt{a^2+b^2-2ab\cos\theta}}{2a} \end{bmatrix}^T}_{J^T} \begin{bmatrix} F^x_{ext} \\ \\ F^y_{ext} \end{bmatrix} \tag{4.1}$$

with J being the Jacobian matrix relating the end-effector velocities $\begin{bmatrix} \dot{x} & \dot{y} \end{bmatrix}$ to the joint velocities $\begin{bmatrix} \dot{d} & \dot{l} \end{bmatrix}$. A simple analysis can be carried out to calculate maximum joint forces required from the mechanism. To this end, it is assumed that the tissue interaction forces are concentrated at the midpoints of the plates. The maximum joint forces resulting from the application of a force of $5N$ over all possible directions in the range of 0-180 degrees (see the frame in Fig. 3.6) for all possible joint configurations is 5N and 3.48N in the lateral (d) and diaphragm (l) directions, respectively.

4.2 Device Model

4.2.1 Valve Model

Proportional pressure regulator valves (Kelly Pneumatics, LFR-15TK-0500-R) are used to supply air to the inflatable diaphragms. Unlike flow rate proportional valves, these valves do not require pressure sensors to measure the chamber pressure. The step response of the valve with outlet pressure range of $0-100\,psi$ is illustrated in Fig. 4.1, where the response time is less than 250ms. According to the pneumatic valve response to the step input, the system can be approximately modeled as a second-order system as follows

$$G_s(s) = \frac{394K_v}{s^2+30s+394} \tag{4.2}$$

that behaves similarly in response to the step input.

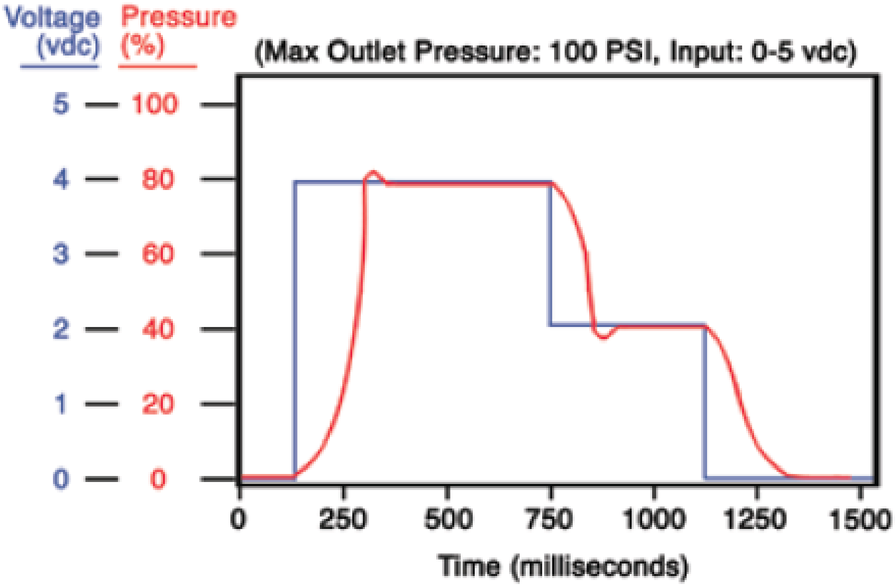

Figure 4.1: Response of pressure regulator valves to a step input. Source: Kelly Pneumatics Product Catalog 2008.

4.2.2 Transmission Line Model

The output ports of the valves are connected to the diaphragm chambers through long transmission lines from MR control room. The basic differential equations governing air flow in a tube are derived in Schuder and Binder (1959),

$$\frac{\partial P(l,t)}{\partial l} = -R_t v - \rho \frac{\partial v}{\partial t} \tag{4.3}$$

$$\frac{\partial v(l,t)}{\partial l} = -\frac{1}{\rho c^2}\frac{\partial P}{\partial t} \tag{4.4}$$

Here P, v and ρ are the air pressure, velocity, and density distribution along transmission line direction l at time t, respectively; R_t is the tube resistance, and c is the speed of sound. It can be shown that P and v satisfy the following second-order partial differential equation, called telegraph equation:

$$\frac{\partial^2 z}{\partial l^2} - \frac{1}{c^2}\frac{\partial^2 z}{\partial t^2} - \frac{R_t}{\rho c^2}\frac{\partial z}{\partial t} = 0 \tag{4.5}$$

where $z = \{v, P\}$ and with different boundary conditions and initial values. In Goldstein (1951), two solutions were found for step and pulse functions as the boundary conditions and with zero initial conditions. However, it is worth noting these differential equations characterize dynamics of an open-end transmission line. For a closed-end transmission line, Yang *et al.* (2011a) used an approximate first-order model with time delay to represent the line dynamics

$$\frac{P_o(s)}{P_i(s)} = \frac{0.25s + 32}{s + 32} e^{-0.0265s} \tag{4.6}$$

where P_o, and P_i are the output and input pressure, respectively; the time delay is the ratio of transmission line length to the speed of sound (L_t/c). This particular transmission line was 9m long with 3.175mm (1/8$in.$) inner diameter. A similar approximate model could be constructed for the transmission line of the device in this thesis. Such models are instrumental in the design of fast feedback control systems where the dynamics of the line must considered to ensure closed-loop stability and good tracking performance. Under quasi-static conditions of operation or in slow feedback control systems, however, the line dynamics may simply be ignored.

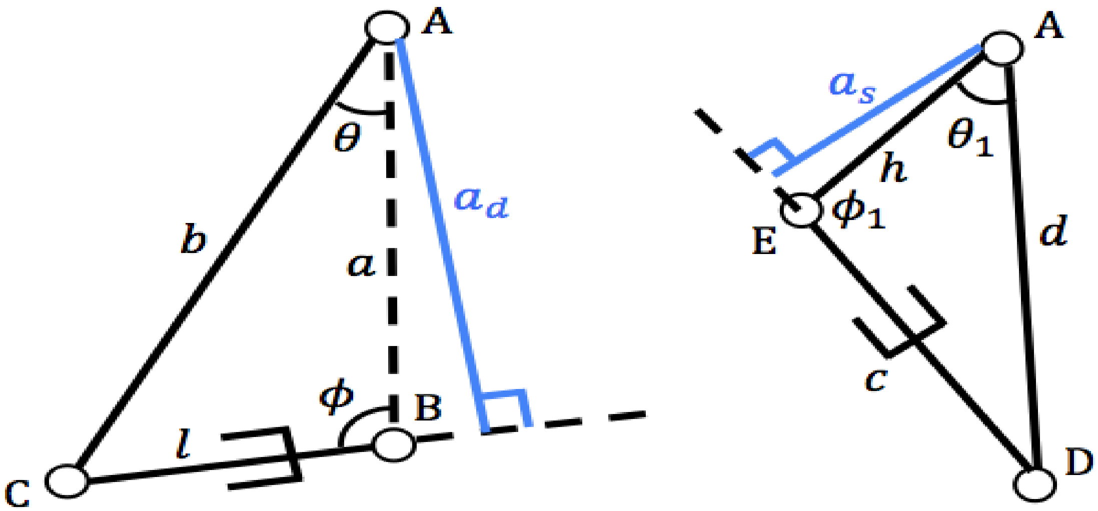

(a) (b)

Figure 4.2: a) Effective arm of diaphragm force about axis A. b) Effective arm of rubber cord force about axis A.

4.2.3 Actuator Model

The top of the diaphragm is attached to an extended surface of the stabilization plate using screw and sealing washer. The diaphragm is folded in an asymmetric shape; therefore, unbalanced radial forces may exist in diaphragm. However, these small forces are neglected to simplify the model. It is assumed that the interaction force between the diaphragm and plate is perpendicular to their interface. The effective pressure area is a circle of 20mm diameter. As a result, the diaphragm force is simply calculated as

$$F_d = \pi R^2 P_o \qquad R = 10mm \tag{4.7}$$

With the plate rotating around around axis A (Fig. 3.6b), the effective arm of the diaphragm (a_d) changes as a function of θ, i.e. see Fig. 4.2a,

$$a_d(\theta) = \frac{ab\sin\theta}{\sqrt{a^2+b^2-2ab\cos\theta}}, \quad 18\theta \leq 40eq:arm1 \tag{4.8}$$

A rubber cord is connected between the stabilization plate and the fixed side link. It provides a counter torque to that of the diaphragm and helps move the plate back to its initial configuration. The robber cord can be modelled as a spring with a constant stiffness k. Referring to Fig. 4.2.b, the force of the rubber cord as a function of the joint variable θ is given by

$$F_s(\theta) = F_0 + k\left(\sqrt{h^2+d^2-2hd\cos(\theta_1)} - L_0\right) \tag{4.9}$$

$$k = \tfrac{\Delta F}{\Delta L} = \tfrac{EA}{L}, \quad \theta_1 = \theta + 47 \tag{4.10}$$

where E, A, and L are young modulus, area, and length of the rubber cord, respectively; F_0 is the initial force in the rubber cord corresponding to its initial length L_0. The effective arm for this force around axis A is

$$a_s(\theta) = \frac{hd\sin(\theta_1)}{\sqrt{h^2+d^2-2ab\cos(\theta_1)}} \tag{4.11}$$

The net actuator torque around axis A (τ_A) can be computed as

$$\tau_A = \underbrace{F_d a_d}_{\tau_d} - \underbrace{F_s a_s}_{\tau_s} \tag{4.12}$$

Table 4.1 summarizes the numerical values for the parameters of the device.

Table 4.1: Numerical dimension and workspace values

θ angle	$18 < \theta < 40$
a	$40mm$
b	$50mm$
d	$45mm$
h	$40mm$
k	$1140N/m$
F_0	$0.8N$
L_0	$45.8mm$

4.3 Controller Design

This section briefly discusses a feedback control system for maintaining the breast biopsy target on the needle insertion path. The controller structure is shown in Fig. 4.3. The are two distinct feedback loops in the proposed controller. The outer loop is based on MR imaging feedback and would compare the current target position and the needle path trajectory and would compute a correction command (θ^d_{right} and θ^d_{left}) for the support plates of the breast stabilization device in order to the move the target back to the needle path; this is represented by the block “Planner”.

The planner works on the principle of small changes in the plate configuration

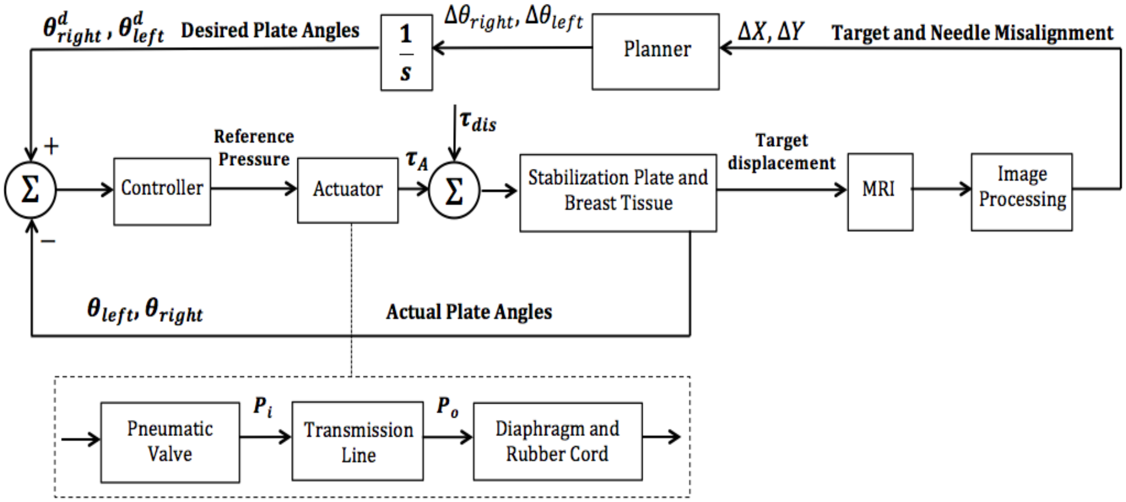

Figure 4.3: The two-level controller structure for biopsy target stabilization.

yielding small changes in the tissue deformation, i.e.

$$\begin{bmatrix} \Delta X \\ \Delta Y \end{bmatrix} = J_c \begin{bmatrix} \Delta\theta_{right} \\ \Delta\theta_{left} \end{bmatrix} \tag{4.13}$$

Here J_c is a Jacobian matrix that defines the relation between the displacement of a point inside tissue (ΔX and ΔY) and changes in the angles of the support plates ($\Delta\theta_{left}$ and $\Delta\theta_{right}$). The computation of this Jacobian matrix will be discussed later in this section.

4.3.1 Control Strategies

Two control strategies for the outer loop feedback system are examined in this thesis, i.e. see Fig. 4.4, although other approaches are also possible. The first strategy involves a single adjustment of the support plates prior to the insertion of the biopsy

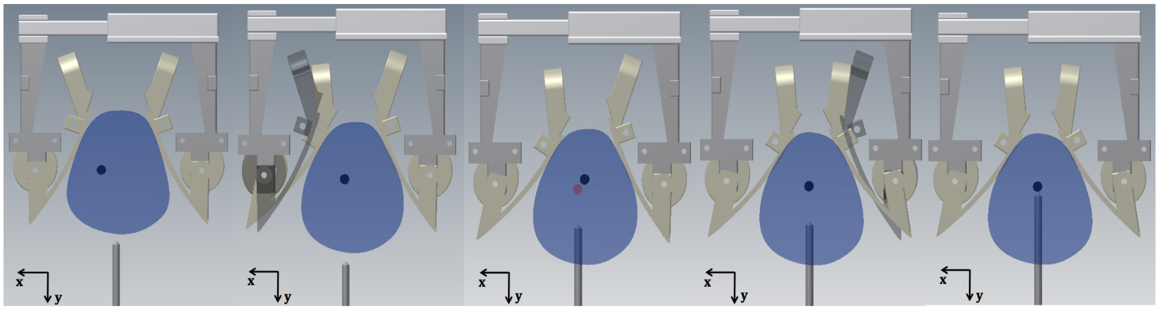

(a) (b) (c) (d) (e)

Figure 4.4: Control strategies for stabilizing biopsy target movements. Note that the first strategy only involves (a), (b) and (e) whereas the second strategy includes all the steps. a) The support plates and the needle insertion mechanism are manually positioned around patient's breast. An MR image is acquired to compute needle targeting error along the x. b) The plates configuration is changed using the pneumatic actuators based the Jacobian relation to move the target on back on the needle insertion path; previous position of the support plate is shown in black. c) The needle is inserted halfway through the tissue and then another image is taken to determine the target displacement due to the needle insertion forces; previous position of target is shown in red. d) Plates configuration is re-adjusted to compensate for any possible target movement; previous position of plate is shown in black. e) The needle insertion is resumed to reach the target.

needle, as described below:

1. The support plates and the needle insertion mechanism are manually positioned around the patient's breast based on data from a diagnostic MR image, which would roughly identify the target location.

2. The patient is moved into the MR imager and another image is acquired to determine misalignment of the target and needle along x (ΔX) and z axes. The z component error would be directly compensated for by the needle drive mechanism.

3. The desired adjustments for the support plates are calculated using

$$\begin{bmatrix} \Delta\theta_{right} \\ \Delta\theta_{left} \end{bmatrix} = J_c^{-1} \begin{bmatrix} \Delta X \\ 0 \end{bmatrix} \tag{4.14}$$

4. A confirmation image is taken and the needle is inserted along the y axis; the insertion depth is determined from the MR image.

Although the shape of the support plates is optimized to minimize target displacement due the forces of the needle, some moderate target displacement is still expected during the needle insertion. In the second control strategy, the support plates would be readjusted a second time halfway through the biopsy based information from another intra-operative image. In this approach:

1. Steps 1-3 of the first strategy are repeated.
2. The plates are adjusted and the needle is inserted halfway through the tissue.
3. An image is taken to determine the target displacements due to the needle insertion forces.
4. Using the target displacements along the x (ΔX) and the y (ΔY) axes and the inverse of the Jacobian, the required changes in the angles of plates are calculated to compensate for the target movement.
5. The needle insertion is resumed to reach the target; the final insertion depth is determined from the second MR image.

4.3.2 Computation of the Jacobian Matrix

Numerical simulations using the deformation model of the breast in Section 3.2 were carried out to compute the Jacobian matrix in (4.13) at different plate configurations and target locations. The results were validated with experiments on chicken breast tissue using electromagnetic position tracking sensor placed inside the tissue while the plate angles were changed independently. To simplify the controller implementation, the values of the Jacobian matrix were averaged over different target locations and plate configurations. The results of closed-loop control experiments with this average Jacobian matrix, which will be discussed later in the thesis, demonstrated the effectiveness of the control strategies with a constant Jacobian matrix.

The inner feedback loop involves two independent joint-level PID controllers that act on the errors between the desired plate angles, computed from the outer loop controller, and the actual angles measured by the optical encoder. It should be noted the outer feedback loop operates at a much lower update rate than that of the inner loop, if on-the-fly real-time MR imaging is used. Otherwise it only updates once or twice depending on the control strategy employed. The outputs of the PID controllers are sent to the two pressure regulator valves with the dynamic response in Fig. 4.1. Yang *et al.* (2011a) demonstrated effectiveness of PI controllers in position control using pressure valves. Here a derivative term is also added to to improve the settling time of the closed-loop response. The output of the pressure regulator valves are connected to the diaphragm chambers through two transmission lines. Note that due to the inclusion of an integral term in the inner joint-level controller, the steady-state joint tracking errors are expected to converge to zero even in the presence of a constant disturbance load (τ_{dis}).

4.4 Frequency Response of Closed-loop System

To determine the accuracy of the controller system to follow desired commands, the frequency response of the closed-loop system can be analyzed. The frequency response is analyzed for the inner feedback control system with the feedback around the joint positions that controls the plates orientations. Estimating the frequency response for a physical system generally involves exciting the system with an input signal, measuring both input and output signals, and comparing the two through a process such as the Fast Fourier Transform (FFT). Alternatively, a model based approach could be pursued where analytical models of the system components can be used to develop a closed-loop transfer function; this is the approach taken in this thesis. Obviously, transfer functions and frequency response analysis are only valid for linear time invariant systems. In this thesis, a linearized model of the actuator system around an operating point is used for such analysis.

To calculate the frequency response for the system (Fig. 4.3), the transfer function ($G(s)$) between the output angle (θ) and the reference signal ($\theta^d - \theta$) must be known. Transfer function for the controller block ($G_1(s)$) is

$$G_1(s) = K_p + \frac{K_I}{s} + K_d s \tag{4.15}$$

According to the pneumatic valve response to the step input (Fig. 4.1), the pneumatic valve block ($G_2(s)$) is approximately modeled as a second-order system given in (4.2), where K_v is the proportional gain of the valve. The transmission line transfer function ($G_3(s)$) for a $9m$ long transmission line with $3.175mm$ inner diameter is similar to the approximation given in (4.6). The controller system is non-linear. The actuator

Table 4.2: Numerical values for the controller system parameters

θ angle	$18 < \theta < 40$
K_p	200
K_I	1000
K_d	5
K_v	$25.25\,Pa$
M	$30.34\ kg.mm^2 rad^-1$
b_f	$0.03\ Nms^2 rad^-1$

torque is a function of the input pressure (P_o) and the plate orientation (θ). Therefore, to calculate the system frequency response the actuator block is linearized around a working point of $\theta_0 = 26°$ and $P_0 = 3.87psi$ and the transfer function is then derived.

$$\tau_A(\theta, P_o) = \underbrace{F_d(P_o)a_d(\theta)}_{\tau_d} - \underbrace{F_s(\theta)a_s(\theta)}_{\tau_s} \tag{4.16}$$

$$\frac{\partial \tau_A}{\partial \theta} = F_d \frac{\partial a_d}{\partial \theta} - F_s \frac{\partial a_s}{\partial \theta} - \frac{\partial F_s}{\partial \theta} a_s \tag{4.17}$$

$$\frac{\partial \tau_A}{\partial P_o} = \pi R^2 a_d \tag{4.18}$$

$$\tau_A = \tau_{nominal} + \frac{\partial \tau_A}{\partial \theta}(\theta - \theta_0) + \frac{\partial \tau_A}{\partial P_o}(P - P_0) \tag{4.19}$$

Using the stabilization plate mechanical model and ignoring the breast tissue inertia, the output angle (θ) is calculated as

$$\frac{\theta(s)}{\tau_A(s)} = \frac{1}{Ms^2 + b_f s} \tag{4.20}$$

where M is the plate moment of inertia and b is torsional damping coefficient. The value of M is calculated using the system CAD model whereas b is estimated according to device properties. Table 4.2 summarizes the numerical values for the parameters of the controller system. $G(s)$ is the open-loop transfer function between the output angle (θ) and the reference signal ($\theta^d - \theta$) and the actuator closed-loop transfer function is given by

$$\frac{\theta(s)}{\theta^d(s)} = H(s) = \frac{G}{1+G} \tag{4.21}$$

Fig. 4.5 illustrates the Bode plot of the open-loop system $G(s)$ while Fig. 4.6 shows its Nyquist diagram. According to the minimum stability margins, the closed-loop system is stable with a phase margin of 66.3° at $3.11 rad/s$ frequency and gain margin of $13.5dB$ at $11.7 rad/s$. The frequency response of the closed-loop system is also shown in Fig. 4.7

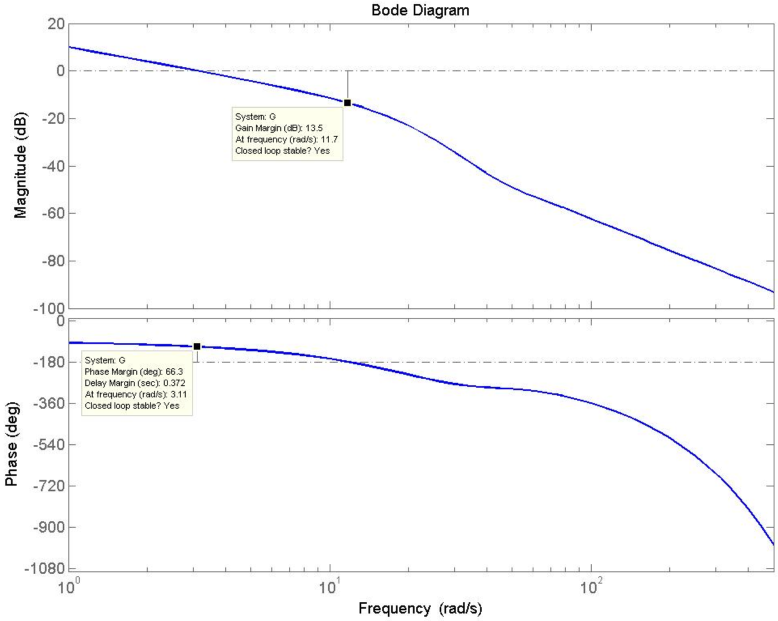

Figure 4.5: Bode plot of the open-loop system $G(s)$.

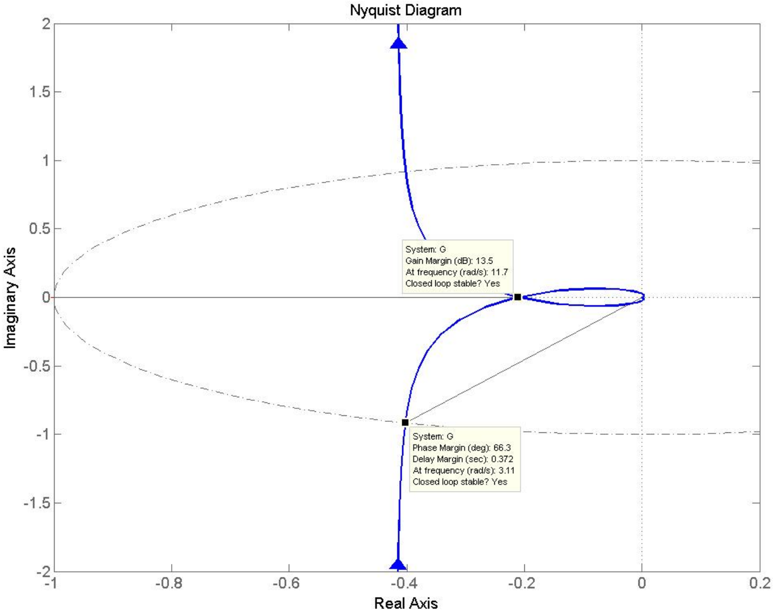

Figure 4.6: Nyquist plot of the open-loop system $G(s)$.

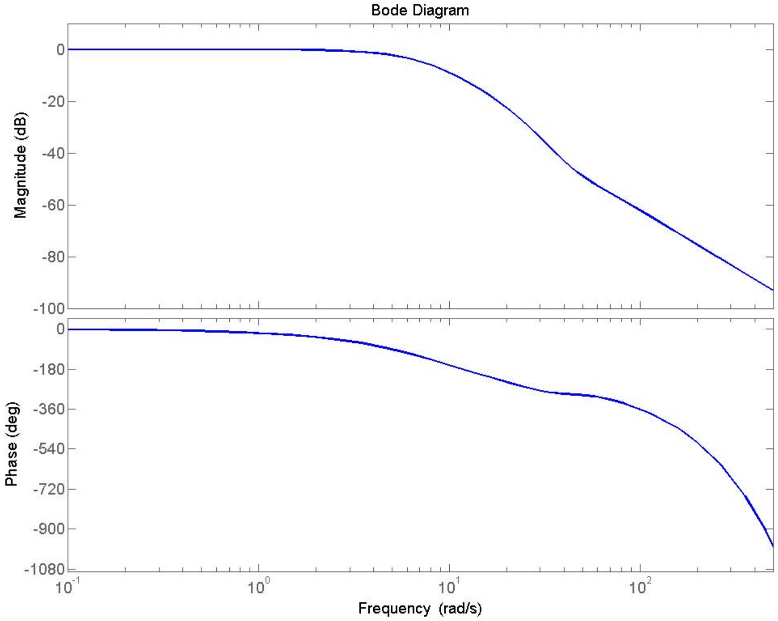

Figure 4.7: Frequency response of the closed-loop system $H(s)$.

Chapter 5

System Evaluation and Experiments

Needle insertion experiments were performed using a prototype of the pneumatically-actuated device in order to evaluate its effectiveness in stabilization of a target inside soft tissue; chicken breast tissue was used in the tests. Miniaturized electromagnetic sensors (Ascension Technology Corporation - 3D Guidance trakSTAR$^{\mathrm{TM}}$- 0.11 mm resolution) were employed as targets to monitor the displacements. The test setup, shown in Fig. 5.1, included two Thermo CRS robots instrumented with force sensors; one of the robots was used to drive the needle while the other applied the preloader. Electromagnetic position sensors were attached to the needle and the support plates to track their movements. Another sensor was inserted inside the tissue as the target. The sensors were small enough that the influence of their size on the results could be neglected. A $3.2mm$ carbon fiber rod with sharpened tip was utilized as needle to avoid interference with the electromagnetic sensors. Two pieces of chilled chicken breasts weighing around $1.2lb$ were placed inside Ziploc®bag. The support plates in the stabilization device were initially positioned at 26°. The lateral distance between the plates was selected such that the tissue filled the entire space inside the stabilization device.

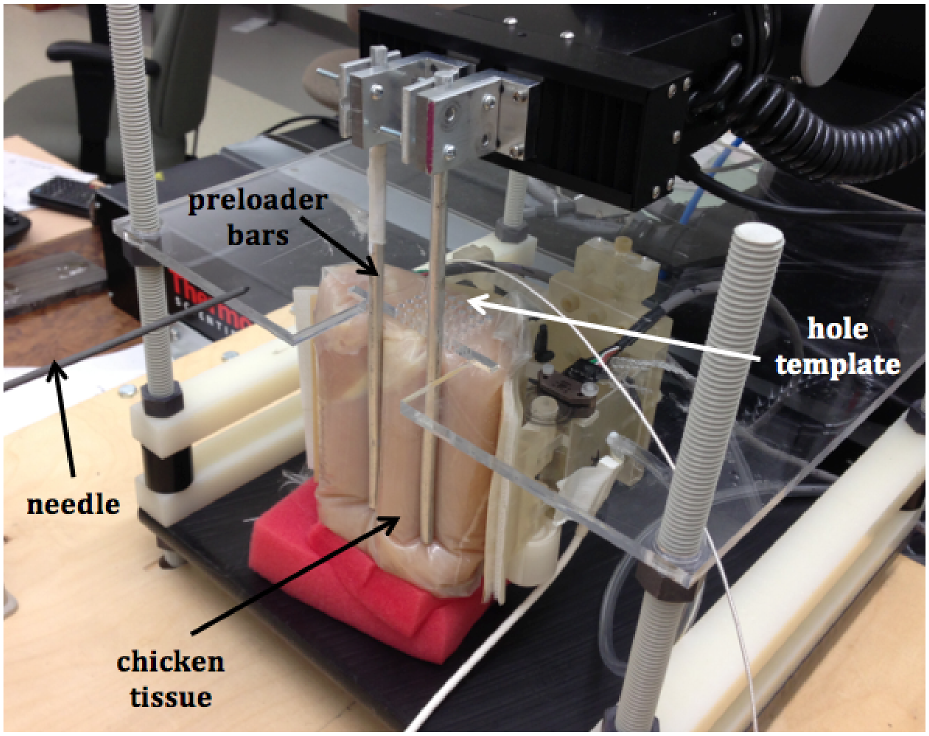

Figure 5.1: Test setup for the needle insertion experiments.

5.1 Test Procedures

Two different test procedures corresponding to the control strategies described in Section 4 were designed to evaluate the stabilization device performance. The protocol for the first experiment is summarized below.

1. Target sensor is inserted inside the tissue through one of the holes in a template, as explained later in the thesis.

2. The needle position is manually offset from the target perpendicular to the insertion trajectory(x axis in Fig. 3.2). The offset values are selected randomly in the range of 1-5mm in both positive and negative directions.

3. The plate configurations are adjusted using feedback control as described in Chapter 4 to bring the target back on the needle insertion path.

4. The needle is inserted along the y axis until its tip reaches the target sensor.

5. The needle is retracted and the procedure is repeated through another hole in the template to cover different regions of the tissue.

The second experiment included all the steps of the first experiment. Additionally, the tissue support plates were re-adjusted a second time halfway through the insertion to compensate for any target displacement due to the needle insertion forces. Under similar conditions, needle insertion tests were also performed without any active adjustments of the support plates for comparison purposes. Finally, an experiment was carried out using a conventional parallel plates system configuration. During the experiments, target points were selected using a template to ensure consistency among different tests. Each chicken breast bag was used for a limited time and number of insertions, as the tissue would start to slowly degenerate in room temperature, and previous needle insertion paths might affect the outcome of the test.

5.2 Error Correction and Target Stabilization

The target displacement (TD) is defined as

$$TD \triangleq \sqrt{(x_f - x_i)^2 + (y_f - y_i)^2 + (z_f - z_i)^2} \tag{5.1}$$

where i and f subscripts refer to the initial and final positions of the target, respectively. The initial target position is defined as the position of target before the start of needle insertion, i.e. the end of the step in Fig. 4.4b; the final target position refers to the position of the target at the end of insertion phase, i.e. the end of the step in Fig. 4.4e.

Fig. 5.2 shows the histograms of the target displacements for each of the control strategies. Table 5.1 reports values for the mean and maximum target displacements. Also, the target compliance is calculated as the ratio of total target displacement to needle insertion force in order to normalize displacement among various tests. Note that the results for the first control strategy are similar to those from an experiment with the passive device with optimal plate shape, i.e. see Table 3.3. This should not be surprising as the first control strategy essentially aligns the the target with the needle path and then merely relies on the plates geometry for target stabilization during needle insertion. The data in Table 5.1 indicates that the second control strategy significantly reduces the target displacement by re-adjusting the plates configuration midway through the insertion. The mean and the maximum of target displacement are substantially lower than those in the first control strategy; this is mainly due to the applied insertion forces in the last phase of needle insertion. Needle insertion forces were recorded to be in $4.1 \pm 0.95N$ range in these experiments.

Table 5.1: Experimental Results

	Mean Target Displacement $[mm]$	Max Target Displacement $[mm]$	Mean Target Compliance $[mm/N]$
One Adjustment Strategy	1.35	2.61	0.12
Two Adjustment Strategy	0.48	1.20	0.10

In the first control strategy, any misalignment of the target and the needle along the x axis will be compensated for by adjusting the plates configurations. Target misalignment is defined as the target offset from the needle axis along the x direction. Table 5.2 reports target misalignment values before and after changing the plates configuration. The corresponding histograms for this data are given in Fig. 5.3. It is clear from the results of the experiment that the control strategy is very effective in aligning the target with the needle insertion path. Fig. 5.4 illustrates two target alignment scenarios in which initial misalignments between the target and needle along the x axis are compensated for by adjusting the support plates. Fig. 5.4a shows a scenario where the plates configuration was adjusted to compensate for the $+5mm$ misalignment between the target and the needle along x axis. Fig. 5.4c illustrates the corresponding motion of the target along y axis as a result of the performed adjustment. Figs. 5.4b and 5.4d exhibit a similar scenario where a $-3mm$ initial misalignment was corrected.

Fig. 5.5 depicts two needle insertion scenarios from the first control strategy. Fig. 5.5a illustrates a needle insertion scenario where a $1.5mm$ misalignment along

Table 5.2: Target misalignment along x axis in the first control strategy before and after the plates adjustment

	Mean Error [mm]	Max Error [mm]
Before the Adjustment	3.24	6.10
After the Adjustment	0.18	0.83

x axis between the target and the needle was compensated by plates adjustment in P1 phase. P2 phase demonstrates the needle insertion and the change in x and y positions of the target due to the insertion forces. The target then returned to its initial position after the needle was retracted in phase P3. Fig. 5.5c shows the needle position along y axis where its movement during the insertion and retraction phases, P2 and P3 respectively, can be seen. Figs. 5.5b and 5.5d exhibit a similar scenario.

Fig. 5.6 depicts two needle insertion scenarios from the second control strategy. During an insertion scenario with the second control strategy (Fig. 5.6a), P1 phase represents the first adjustment of the plates to correct for the initial misalignment ($2.8mm$) of the needle and the target along x axis. The needle insertion is performed halfway through the tissue during phase P2 and the corresponding target movement is illustrated. A second adjustment of the plates is performed in phase P3 where the target is pushed back toward its initial position before the start of the insertion. The insertion is then resumed in phase P4 until the tip of the needle reaches the target position and the needle is retracted in phase P5. Fig. 5.6c shows the corresponding y position of the needle tip during these phases. Another similar scenario is illustrated in Figs. 5.6b and 5.6d where an initial misalignment of $-4mm$ between the needle and the target is corrected by the first adjustment of the support plates before and the second adjustment compensates for the target displacement after the needle is halfway inserted.

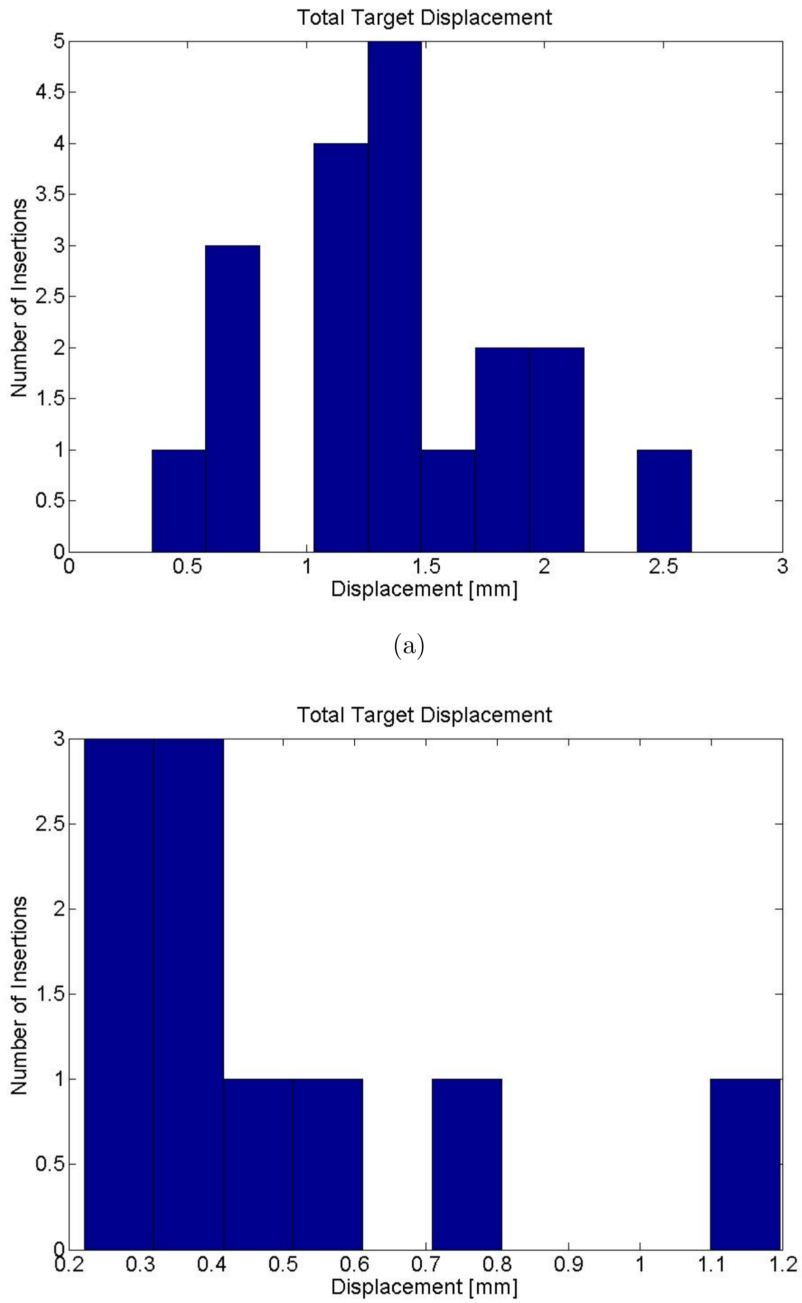

(a)

(b)

Figure 5.2: Mean of total target displacement for a) first control strategy b) second control strategy.

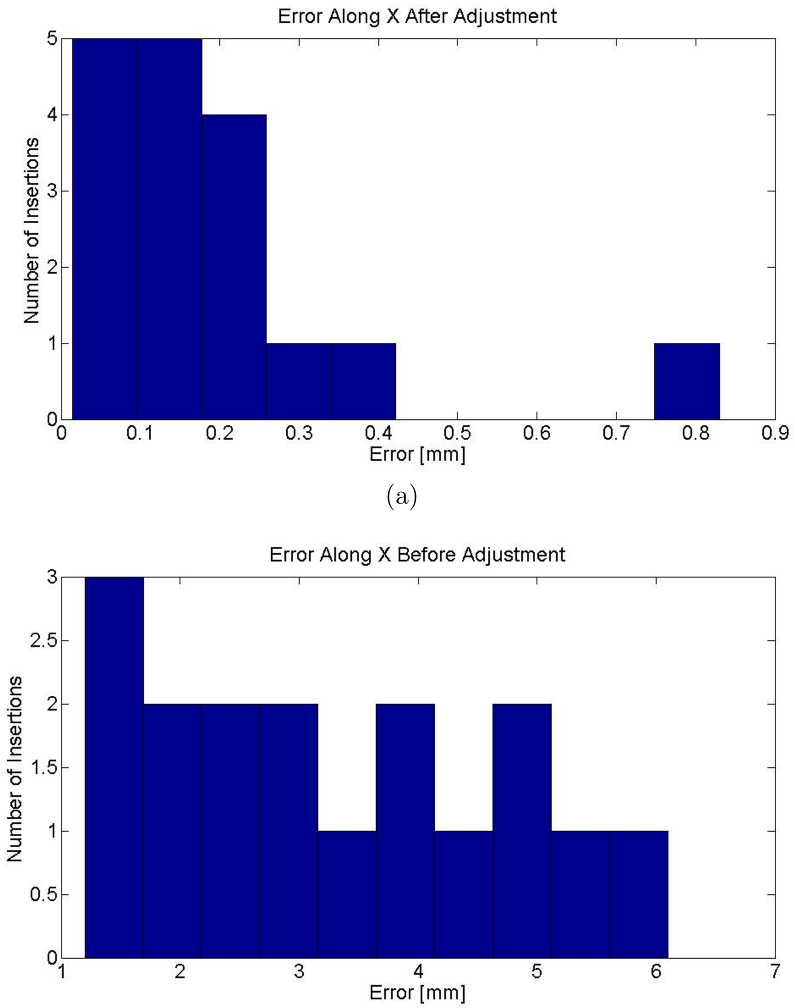

(a)

(b)

Figure 5.3: Needle and target misalignment along the x axis in the first control strategy: a) before plates adjustment; b) after plates adjustment.

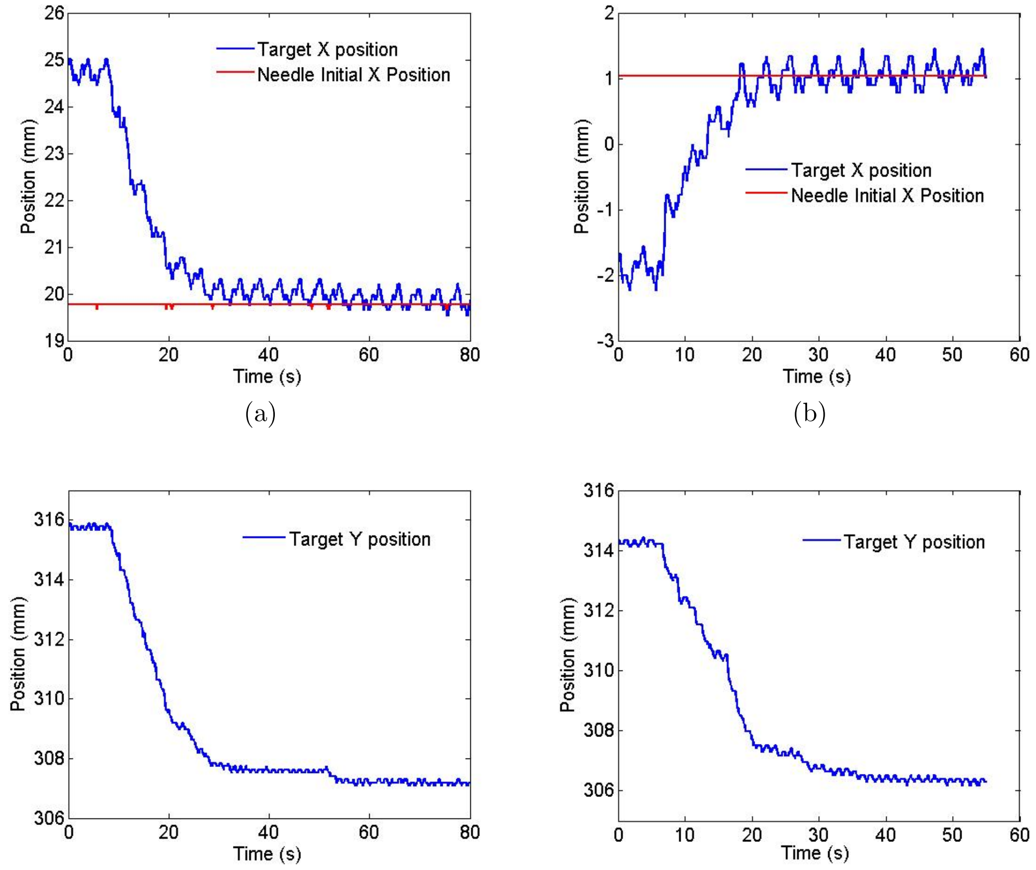

(a) (b)

(c) (d)

Figure 5.4: Correction of target and needle misalignment in x direction using the first control strategy: (a), (c) Scenario I; (b), (d) Scenario II.

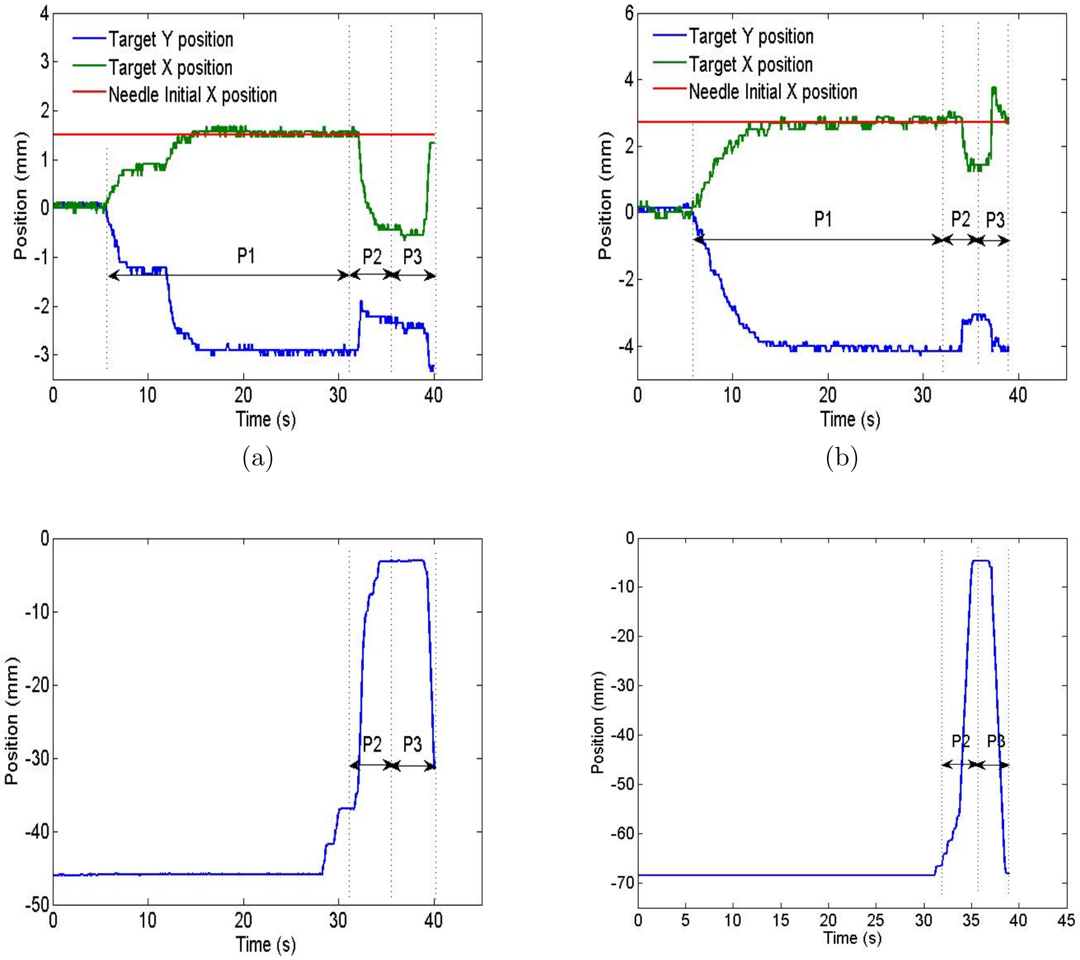

(a) (b) (c) (d)

Figure 5.5: Two test scenarios with the first control strategy: a), b) target x and y positions and needle position along x axis. c), d), needle position along the insertion path. Different phases are: P1- One adjustment of plates. P2-Needle insertion. P3-Needle retraction.

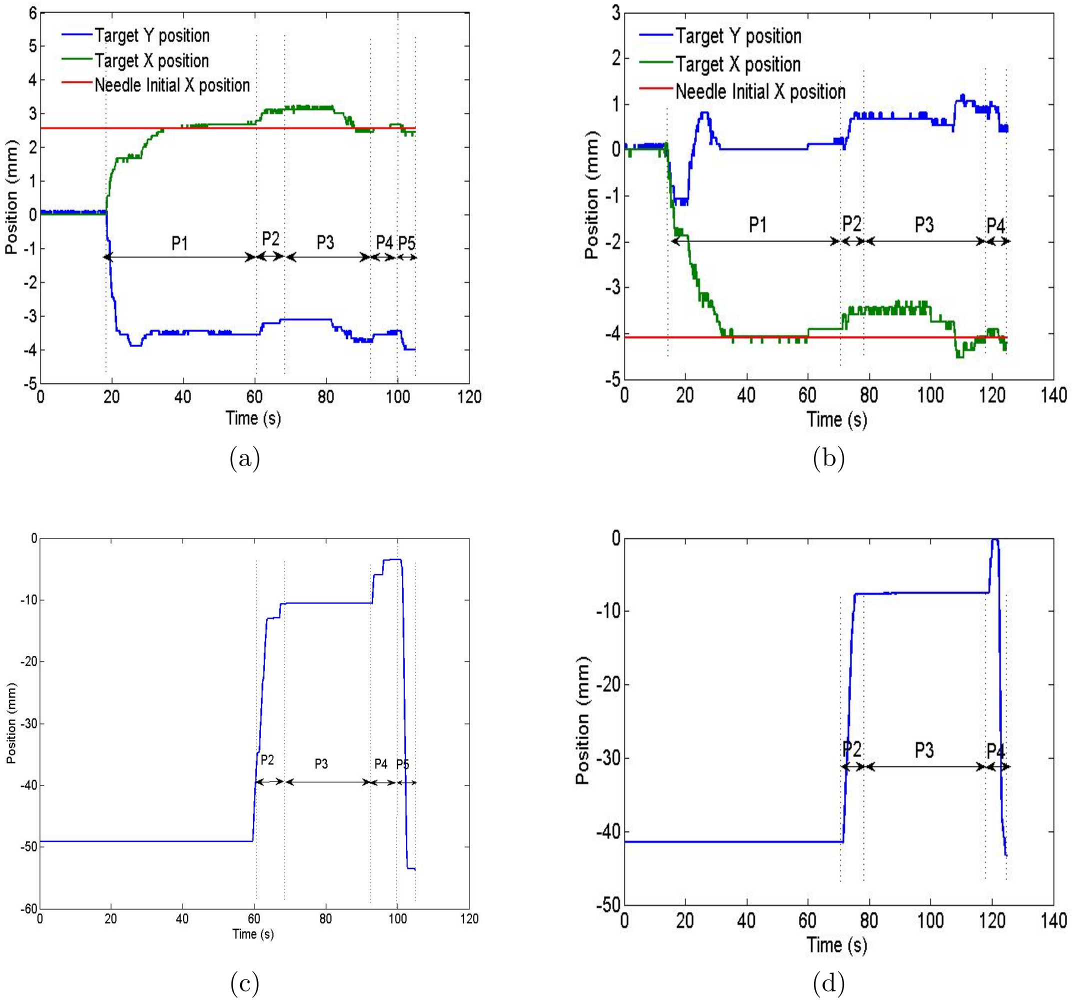

Figure 5.6: Two test scenarios with the second control strategy: a), b) target x and y positions and needle position along x axis. c), d), needle position along the insertion path. Different phases are: P1- First adjustment of plates. P2-Needle insertion halfway through. P3-Second adjustment of plates. P4-Needle insertion and retraction.

5.3 MRI Compatibility

The tissue stabilization device was tested inside MRI to examine its compatibility. The experimental setup, illustrated in Fig. 5.7, shows the device inside a 3 Tesla MRI magnet bore. The pneumatic valves were located outside of the MRI room and air was supplied using long transmission lines that passed through a waveguide panel. A USB-based US Digital board (USB4 Encoder Data Acquisition USB Device) was used for sending the control commands to the valves and reading the optical encoder signals. The encoders signals were also sent out to the control room through the waveguide; however, the power lines for the encoders remained inside the MRI room and the encoders were powered by batteries. The circuits on the encoder and data acquisition board sides were electrically isolated from each other using optocouplers. The imaging sequence used was 3-D Fast SPGR (Spoiled Gradient Echo), with TE=1.4 ms, TR=5.1 ms, and slice thickness=1 mm. The phantom used in the imaging (GE Healthcare, dimension: $49x66x168mm$) was made of water with nickel chloride in order to shorten the relaxation times (T1 and T2) of the water. The device was imaged in different configurations to assess MR image quality and the device performance inside the imagining machine:

1. Device was inside the MR bore with the encoders powered off.
2. Encoders were powered on.
3. Device was actuated during image acquisition.

The MR images were assessed using the non-medical version of OsiriX software. The signal to noise ratio (SNR) in the MR images were calculated in different configurations to examine the device influence on image quality. As can be seen in Fig. 5.8,

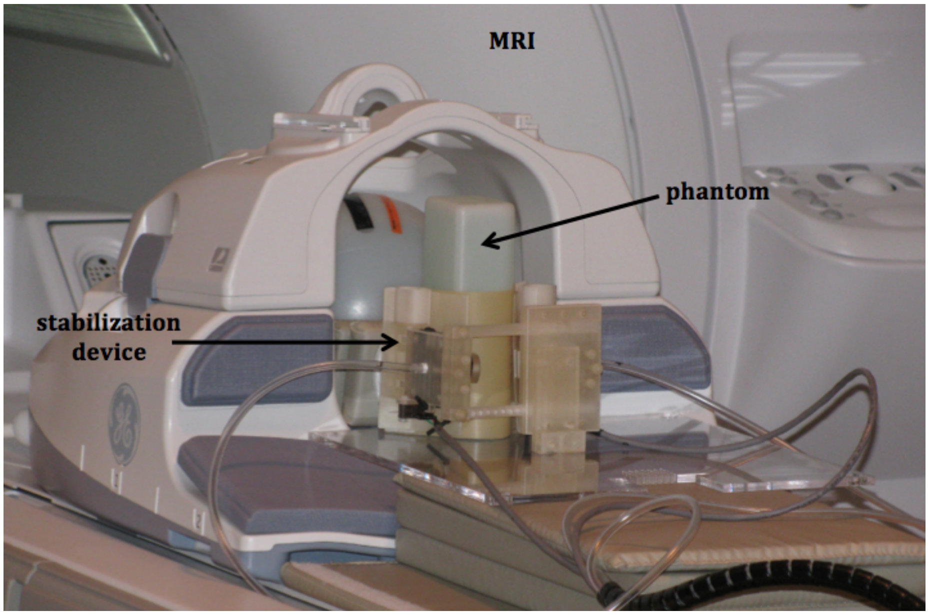

Figure 5.7: Test setup inside MRI.

when powered off, the device has no perceptible impact on the image quality. Powering the encoders introduces some modest noise dropping the SNR value from 54.3 to 40; this represents a 26% drop in the SNR value. Fig. 5.9a shows the results for a case in which the feedback control system of the support plates is active during image acquisition. This scenario resulted in 40% drop in the SNR value to 32.5. A moderate structural noise due to the feedback control system was also observed in this case. In another test configuration, the MRI receiver gain was decreased by 18% (Fig. 5.9b). This resulted in a significant drop in noise and increased the SNR value to 62.9. It should also be pointed out that no significant image distortion was observed in any of the MR-compatibility experiments.

Considering the definition of MR-compatible zones Chinzei *et al.* (1999), the proposed tissue stabilization device is categorized in zone 1, a device that operates inside imaging region of interest. The apparatus is deemed to be MR-compatible as no significant image distortion was observed even during the active movement of the device. While the SNR values dropped by as much as 40% during active feedback control, their values remained in an acceptable range for detecting a lesion location in the MR image; these images are used to detect a target location inside the breast tissue while its approximate location is known from the pre-operative images.

(a) (b)

Figure 5.8: MR images acquired in presence of the stabilization device. a) encoders are powered off. b) encoders are powered on. The green circles represent the regions of the image used in the calculation of the SNR.

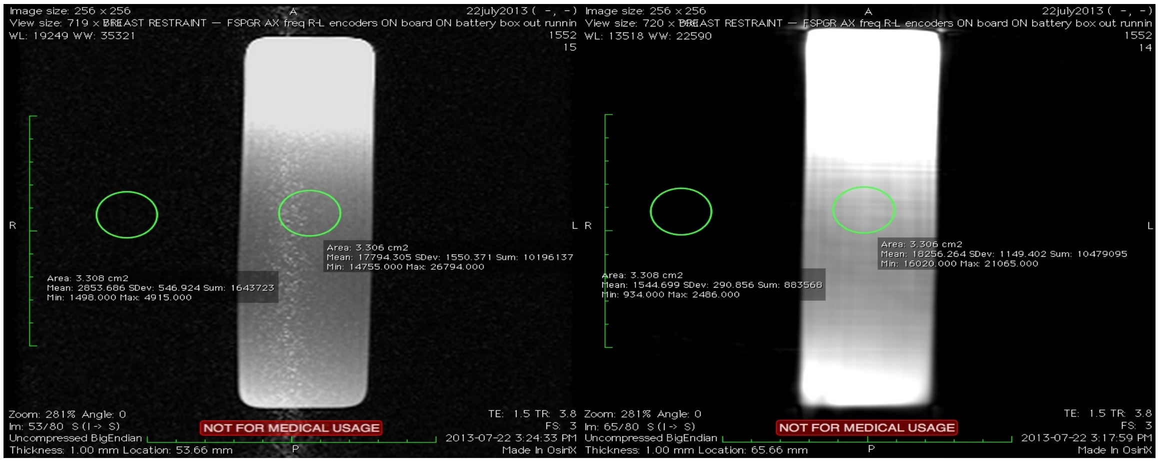

(a) (b)

Figure 5.9: MR images acquired in the presence of stabilization device: a) device moving. b) device moving with lower imager receiver gain. The green circles represent the regions of the image used in the calculation of the SNR.

Chapter 6

Conclusions and Future Work

6.1 Conclusions

This thesis presented novel devices and control methodologies for tissue stabilization in MR-guided breast biopsy procedures. The proposed devices employed piezoelectric (3 DOF) and pneumatic (2 DOF) actuators to allow in magnet MR-guided motion control for biopsy target stabilization. A needle driver mechanism (2 DOF) using piezoelectric actuators was also presented that could be employed in a system along with the tissue stabilization device for MR-guided biopsy intervention.

The tissue stabilization devices consist of two tissue support plates with optimized geometry. These optimally shaped plates provide comparable tissue stabilization compared to that of the conventional parallel plates, at reduced tissue compression forces and patient discomfort. The lower compression forces are expected to help improve the uptake of MRI contrast agent as a result of an increased blood flow, improving the diagnostic MR images quality. The support plates has an open-front configuration that provides greater accessibility and flexibility in selecting the needle insertion trajectory and entry point, which is limited to a fixed grid in the conventional parallel plates configuration. The stabilization plates orientation can be actively controlled using pneumatic or piezoelectric actuation while the piezoelectric-based design offers another active DOF in lateral distance adjustment of plates. This allows for in-bore adjustments to the plates configuration in order to compensate for the movements of the lesion due to the insertion forces as well as initial misalignment of the target and the needle. This capability would reduce the overall procedure time by eliminating the need for multiple transfers of the patient in and out of the magnet and can enhance targeting accuracy.

Two control strategies were proposed for image-based breast biopsy using the new tissue stabilization device. In the first control strategy, one adjustment of the plates configurations is performed based on data from a pre-operative MR image to compensate for the target and the needle error along the frontal axis. In the second control strategy, another adjustment of the support plates is carried out when the needle is halfway inserted in the tissue, which corrects for target displacements along frontal and longitudinal axes due to the insertion forces. An important assumption in proposing the second control strategy is the availability of MR-compatible biopsy needles. Needle insertion experiments with chicken breast tissue were carried out to validate the device functionality and the effectiveness of the image-based control strategies. The results of these experiments showed significant improvements in tissue stabilization and targeting accuracy using the proposed device and control strategies. Experiments performed in an MRI machine demonstrated that while the device may introduce some moderate structural noise and deteriorate the image SNR, it would cause no significant image distortion. The images acquired with the device functioning inside the machine are deemed sufficient for the indented application of this technology. The advantages of the proposed system for MRI-guided breast biopsy can be summarized as follows:

- Comparable tissue stabilization capability of the proposed tissue support plates to that of a parallel plates configuration at reduced patient discomfort.
- Improved target localization capability as a consequence of greater uptake of contrast agent and longer target visibility period.
- Greater flexibility in selecting the needle insertion trajectory and entry point because of the open-front configuration of the support plates.
- Improved target positioning accuracy as result of active adjustments of the tissue stabilization plates based on MR feedback.
- Ability to use a simplified needle driver mechanism with at most 2 DOF
- Reduced procedure time via elimination of unnecessary patient transfers in and out of the MRI machine.

6.2 Future Work

The outcomes of the work with the early prototype of the tissue stabilization device point to a number of limitations that need to be addressed in future. While the active adjustments of the plates orientation proved effective in compensating for targeting errors and displacements in the order of a few millimeters, correcting larger errors would require an active control of the lateral position of the plates. A future prototype of the system based on the piezoelectric-based concept design should enable in-bore lateral adjustments of the support plates to enable corrections for larger misalignments in order of few centimeters.

Further work is required to identify the source and eliminate a moderate structural noise that was observed during the MR-compatibility tests. A possible solution to this problem would be to use optical fiber from of the transmission of the encoder signals. Additionally, encoder signals can be transmitted to the MRI control room using the penetration panel. This panel filters the input and output signals of the MRI room for a suitable form of Radio Frequency (RF) shielding to prevent unwanted external signals to penetrate the magnetic shielded room.

Acquired MR images during the MR-compatibility tests were mainly from axial plane of the phantom. To further verify the device MR-compatibility, MR images from other planes of the phantom especially the sagittal plane (pre-operative diagnostic images are usually parallel to sagittal plane) can also be assessed to evaluate the effect of tissue stabilization device operation on these images.

Finally, a prototype of the piezoelectric-based needle drive mechanism can be developed. Integration of linear encoders with fiber-optic form of signal transmission in the custom-made linear bearings, allows for precise motion control of a biopsy gun. In-bore automated needle insertions then can be performed under MR-guidance. The prototype can be integrated with the proposed tissue stabilization device for complete tests inside MRI machine.

Bibliography

ANVARI, M., STEFURAK, L., REEDMAN, T., FIELDING, T. S., SCHMIDT, M. R. M., YEUNG, H. B., RANDALL, K. J., DOBRANOWSKI, J., BOYLAN, C., LEE, L. Q. C., *et al.* (2011). Automated in-bore mr guided robotic diagnostic and therapeutic system. WO Patent 2,011,063,511.

Azar, F. S., Metaxas, D. N., and Schnall, M. D. (2000). A finite element model of the breast for predicting mechanical deformations during biopsy procedures. In *Mathematical Methods in Biomedical Image Analysis, 2000. Proceedings. IEEE Workshop on*, pages 38–45. IEEE.

Azar, F. S., Metaxas, D. N., and Schnall, M. D. (2002). Methods for modeling and predicting mechanical deformations of the breast under external perturbations. *Medical Image Analysis*, **6**(1), 1–27.

Bock, M., Melzer, A., Bardenheuer, H., Ghaderi, H., Gutmann, B., Zimmermann, H., and Semmler, W. (2005). Mr-guided percutaneous interventions using a robotic assistance system: initial experiences in a pig model. In *Proceedings of the 2005 Conference of the International Society for Magnetic Resonance in Medicine, Miami, FL, USA*, pages 2665–2670.

Bogue, R. (2011). Robots in healthcare. *Industrial Robot: An International Journal*, **38**(3), 218–223.

Booker, A. J., Dennis Jr, J., Frank, P. D., Serafini, D. B., Torczon, V., and Trosset, M. W. (1999). A rigorous framework for optimization of expensive functions by surrogates. *Structural optimization*, **17**(1), 1–13.

Chen, M. (2013). *Designing a Tissue Stabilization Device for MRI-Guided Breast Biopsy*. Master's thesis, McMaster University, Hamilton,Canada.

Chinzei, K. and Miller, K. (2000). Towards mri guided surgical manipulator. *Medical science monitor: international medical journal of experimental and clinical research*, **7**(1), 153–163.

Chinzei, K., Kikinis, R., and Jolesz, F. A. (1999). Mr compatibility of mechatronic devices: design criteria. In *Medical Image Computing and Computer-Assisted Intervention–MICCAI99*, pages 1020–1030. Springer.

Chinzei, K., Hata, N., Jolesz, F. A., and Kikinis, R. (2000). Mr compatible surgical assist robot: System integration and preliminary feasibility study. In *Medical Image Computing and Computer-Assisted Intervention–MICCAI 2000*, pages 921–930. Springer.

Choi, H.-S., Han, C.-S., Lee, K.-y., and Lee, S.-h. (2005). Development of hybrid robot for construction works with pneumatic actuator. *Automation in Construction*, **14**(4), 452–459.

Christoforou, E., Akbudak, E., Ozcan, A., Karanikolas, M., and Tsekos, N. V. (2007).

Performance of interventions with manipulator-driven real-time mr guidance: implementation and initial in vitro tests. *Magnetic resonance imaging*, **25**(1), 69–77.

Cramer, S. C., Weisskoff, R. M., Schaechter, J. D., Nelles, G., Foley, M., Finklestein, S. P., and Rosen, B. R. (2002). Motor cortex activation is related to force of squeezing. *Human brain mapping*, **16**(4), 197–205.

Debatin, J. F. and Adam, G. (1998). *Interventional magnetic resonance imaging*. Springer Berlin.

Del Palomar, A. P., Calvo, B., Herrero, J., Lopez, J., and Doblaré, M. (2008). A finite element model to accurately predict real deformations of the breast. *Medical engineering & physics*, **30**(9), 1089–1097.

Deurloo, E. E., Gilhuijs, K. G., Kool, L. J. S., and Muller, S. H. (2001). Displacement of breast tissue and needle deviations during stereotactic procedures. *Investigative radiology*, **36**(6), 347–353.

Elhawary, H., Zivanovic, A., Davies, B., and Lamperth, M. (2006). A review of magnetic resonance imaging compatible manipulators in surgery. *Proceedings of the Institution of Mechanical Engineers, Part H: Journal of Engineering in Medicine*, **220**(3), 413–424.

Gassert, R., Moser, R., Burdet, E., and Bleuler, H. (2006). Mri/fmri-compatible robotic system with force feedback for interaction with human motion. *Mechatronics, IEEE/ASME Transactions on*, **11**(2), 216–224.

Goldfischer, M. (2010). Mri-guided breast biopsy. *Applied Radiology*, **39**(3), 28.

Goldstein, S. (1951). On diffusion by discontinuous movements, and on the telegraph equation. *The Quarterly Journal of Mechanics and Applied Mathematics*, **4**(2), 129–156.

Graessle, D., Oslan, A. L., Venditti, S. D., Becht, G., Hass, M. A., *et al.* (2007). Breast magnetic resonace imaging system with curved breast paddles. US Patent 7,171,256.

Harvey, J. A., Moran, R. E., and DeAngelis, G. A. (2000). Technique and pitfalls of ultrasound-guided core-needle biopsy of the breast. In *Seminars in Ultrasound, CT and MRI*, volume 21, pages 362–374. Elsevier.

Haslinger, J. and Mäkinen, R. A. (2003). *Introduction to shape optimization: theory, approximation, and computation*, volume 7. Siam.

Hempel, E., Fischer, H., Gumb, L., Höhn, T., Krause, H., Voges, U., Breitwieser, H., Gutmann, B., Durke, J., Bock, M., *et al.* (2003). An mri-compatible surgical robot for precise radiological interventions. *Computer Aided Surgery*, **8**(4), 180–191.

Kaiser, W. A., Fischer, H., Vagner, J., and Selig, M. (2000). Robotic system for biopsy and therapy of breast lesions in a high-field whole-body magnetic resonance tomography unit. *Investigative Radiology*, **35**(8), 513–519.

Keeler, E. K., Casey, F. X., Engels, H., Lauder, E., Pirto, C. A., Reisker, T., Rogers, J., Schaefer, D. J., and Tynes, T. (1998). Accessory equipment considerations with respect to mri compatibility. *Journal of Magnetic Resonance Imaging*, **8**(1), 12–18.

Khanicheh, A., Muto, A., Triantafyllou, C., Weinberg, B., Astrakas, L., Tzika, A., and Mavroidis, C. (2005). Mr compatible erf driven hand rehabilitation device.

In *Rehabilitation Robotics, 2005. ICORR 2005. 9th International Conference on*, pages 7–12. IEEE.

Kim, D., Kobayashi, E., Dohi, T., and Sakuma, I. (2002). A new, compact mr-compatible surgical manipulator for minimally invasive liver surgery. In *Medical Image Computing and Computer-Assisted InterventionMICCAI 2002*, pages 99–106. Springer.

Kobayashi, Y., Suzuki, M., Kato, A., Hatano, M., Konishi, K., Hashizume, M., and Fujie, M. G. (2012). Enhanced targeting in breast tissue using a robotic tissue preloading-based needle insertion system. *Robotics, IEEE Transactions on*, **28**(3), 710–722.

Kopans, D. B. (1992). The positive predictive value of mammography. *AJR. American journal of roentgenology*, **158**(3), 521–526.

Krautkrämer, J. and Krautkrämer, H. (1990). Ultrasonic testing of materials.

Krieger, A., Susil, R. C., Ménard, C., Coleman, J. A., Fichtinger, G., Atalar, E., and Whitcomb, L. L. (2005). Design of a novel mri compatible manipulator for image guided prostate interventions. *Biomedical Engineering, IEEE Transactions on*, **52**(2), 306–313.

Kuhl, C. K., Schmutzler, R. K., Leutner, C. C., Kempe, A., Wardelmann, E., Hocke, A., Maringa, M., Pfeifer, U., Krebs, D., and Schild, H. H. (2000). Breast mr imaging screening in 192 women proved or suspected to be carriers of a breast cancer susceptibility gene: Preliminary results1. *Radiology*, **215**(1), 267–279.

Kuhl, C. K., Schrading, S., Bieling, H. B., Wardelmann, E., Leutner, C. C., Koenig, R., Kuhn, W., and Schild, H. H. (2007). Mri for diagnosis of pure ductal carcinoma in situ: a prospective observational study. *The Lancet*, **370**(9586), 485–492.

Larson, B. T., Erdman, A. G., Tsekos, N. V., Yacoub, E., Tsekos, P. V., Koutlas, I. G., *et al.* (2004). Design of an mri-compatible robotic stereotactic device for minimally invasive interventions in the breast. *Journal of biomechanical engineering*, **126**(4), 458–465.

LaTrenta, L. R., Menell, J. H., Morris, E. A., Abramson, A. F., Dershaw, D. D., and Liberman, L. (2003). Breast lesions detected with mr imaging: Utility and histopathologic importance of identification with us1. *Radiology*, **227**(3), 856–861.

Lehman, C. D., Gatsonis, C., Kuhl, C. K., Hendrick, R. E., Pisano, E. D., Hanna, L., Peacock, S., Smazal, S. F., Maki, D. D., Julian, T. B., *et al.* (2007). Mri evaluation of the contralateral breast in women with recently diagnosed breast cancer. *New England Journal of Medicine*, **356**(13), 1295–1303.

Liberman, L., Morris, E. A., Dershaw, D. D., Thornton, C. M., Van Zee, K. J., and Tan, L. K. (2003). Fast mri-guided vacuum-assisted breast biopsy: initial experience. *American Journal of Roentgenology*, **181**(5), 1283–1293.

Lufkin, R. B. (1999). *Interventional MRI.* Mosby Inc.

Mallapragada, V., Sarkar, N., and Podder, T. K. (2007). A robotic system for real-time tumor manipulation during image guided breast biopsy. In *Bioinformatics and Bioengineering, 2007. BIBE 2007. Proceedings of the 7th IEEE International Conference on*, pages 204–210. IEEE.

Masamune, K., Kobayashi, E., Masutani, Y., Suzuki, M., Dohi, T., Iseki, H., and Takakura, K. (1995). Development of an mri-compatible needle insertion manipulator for stereotactic neurosurgery. *Computer Aided Surgery*, **1**(4), 242–248.

Morris, E. A., Liberman, L., and Liberman, L. (2005). Percutaneous magnetic resonance imaging guided breast biopsy. *Breast MRI: Diagnosis and Intervention*, pages 297–315.

Moscatel, M. A., Shellock, F. G., and Morisoli, S. M. (1995). Biopsy needles and devices: Assessment of ferromagnetism and artifacts during exposure to a 1.5-t mr system. *Journal of Magnetic Resonance Imaging*, **5**(3), 369–372.

Mushlin, A. I., Kouides, R. W., and Shapiro, D. E. (1998). Estimating the accuracy of screening mammography: a meta-analysis. *American journal of preventive medicine*, **14**(2), 143–153.

O'Flynn, E., Wilson, A., and Michell, M. (2010). Image-guided breast biopsy: state-of-the-art. *Clinical radiology*, **65**(4), 259–270.

Okazawa, S., Ebrahimi, R., Chuang, J., Salcudean, S. E., and Rohling, R. (2005). Hand-held steerable needle device. *Mechatronics, IEEE/ASME Transactions on*, **10**(3), 285–296.

Parker, S., Jobe, W. E., Dennis, M. A., Stavros, A., Johnson, K., Yakes, W., Truell, J., Price, J., Kortz, A., and Clark, D. (1993). Us-guided automated large-core breast biopsy. *Radiology*, **187**(2), 507–511.

Pathmanathan, P., Gavaghan, D., Whiteley, J., Brady, M., Nash, M., Nielsen, P., and Rajagopal, V. (2004). Predicting tumour location by simulating large deformations of the breast using a 3d finite element model and nonlinear elasticity. In *Medical Image Computing and Computer-Assisted Intervention–MICCAI 2004*, pages 217–224. Springer.

Patriciu, A., Petrisor, D., Muntener, M., Mazilu, D., Schar, M., and Stoianovici, D. (2007). Automatic brachytherapy seed placement under mri guidance. *Biomedical Engineering, IEEE Transactions on*, **54**(8), 1499–1506.

Patriciu, A., Chen, M., Iranpanah, B., and Sirouspour, S. (2013). A tissue stabilization device for mri-guided breast biopsy. *Submitted for publication to Medical Engineering & Physics*.

Pfleiderer, S. O., Reichenbach, J. R., Azhari, T., Marx, C., Malich, A., Schneider, A., Vagner, J., Fischer, H., and Kaiser, W. A. (2003). A manipulator system for 14-gauge large core breast biopsies inside a high-field whole-body mr scanner. *Journal of Magnetic Resonance Imaging*, **17**(4), 493–498.

Pfleiderer, S. O., Marx, C., Vagner, J., Franke, R.-P., Reichenbach, J. R., and Kaiser, W. A. (2005). Magnetic resonance-guided large-core breast biopsy inside a 1.5-t magnetic resonance scanner using an automatic system: in vitro experiments and preliminary clinical experience in four patients. *Investigative radiology*, **40**(7), 458–463.

Pijnappel, R., Van den Donk, M., Holland, R., Mali, W. T. M., Peterse, J., Hendriks, J., and Peeters, P. (2004). Diagnostic accuracy for different strategies of image-guided breast intervention in cases of nonpalpable breast lesions. *British journal of cancer*, **90**(3), 595–600.

Plewes, D. B., Bishop, J., Samani, A., and Sciarretta, J. (2000). Visualization and quantification of breast cancer biomechanical properties with magnetic resonance elastography. *Physics in Medicine and Biology*, **45**(6), 1591.

Podo, F., Sardanelli, F., Canese, R., D'Agnolo, G., Natali, P., Crecco, M., Grandinetti, M., Musumeci, R., Trecate, G., Bergonzi, S., *et al.* (2002). The italian multi-centre project on evaluation of mri and other imaging modalities in early detection of breast cancer in subjects at high genetic risk. *Journal of experimental & clinical cancer research: CR*, **21**(3 Suppl), 115–124.

Sarkar, S., Zhang, Y., Qiu, Y., Goldgof, D., and Li, L. (2007). 3d finite element modeling of nonrigid breast deformation for feature registration in-ray and mr images. In *Applications of Computer Vision, 2007. WACV'07. IEEE Workshop on*, pages 38–38. IEEE.

Schenck, J. F. (1998). Mr safety at high magnetic fields. *Magnetic resonance imaging clinics of North America*, **6**(4), 715.

Schenck, J. F. (2000). Safety of strong, static magnetic fields. *Journal of magnetic resonance imaging*, **12**(1), 2–19.

Schuder, C. and Binder, R. (1959). The response of pneumatic transmission lines to step inputs. *Journal of Basic Engineering*, **81**(12), 578–584.

Shellock, F. G. (2000). Radiofrequency energy-induced heating during mr procedures: A review. *Journal of Magnetic Resonance Imaging*, **12**(1), 30–36.

Shellock, F. G. and Crues, J. V. (2004). Mr procedures: Biologic effects, safety, and patient care1. *Radiology*, **232**(3), 635–652.

Shellock, F. G. and Shellock, V. J. (1998). Cardiovascular catheters and accessories: ex vivo testing of ferromagnetism, heating, and artifacts associated with mri. *Journal of Magnetic Resonance Imaging*, **8**(6), 1338–1342.

Smith, M., Zhai, X., Harter, R., Sisney, G., Elezaby, M., and Fain, S. (2008). A novel mr-guided interventional device for 3d circumferential access to breast tissue. *Medical physics*, **35**, 3779.

Society, A. C. (2007). Breast cancer facts & figures 2007-2008.

Stoianovici, D., Song, D., Petrisor, D., Ursu, D., Mazilu, D., Mutener, M., Schar, M., and Patriciu, A. (2007a). mri stealth robot for prostate interventions. *Minimally Invasive Therapy & Allied Technologies*, **16**(4), 241–248.

Stoianovici, D., Patriciu, A., Petrisor, D., Mazilu, D., and Kavoussi, L. (2007b). A new type of motor: pneumatic step motor. *Mechatronics, IEEE/ASME Transactions on*, **12**(1), 98–106.

Susil, R. C., Camphausen, K., Choyke, P., McVeigh, E. R., Gustafson, G. S., Ning, H., Miller, R. W., Atalar, E., Coleman, C. N., and Ménard, C. (2004). System for prostate brachytherapy and biopsy in a standard 1.5 t mri scanner. *Magnetic Resonance in Medicine*, **52**(3), 683–687.

Sutherland, G. R., McBeth, P. B., and Louw, D. F. (2003). Neuroarm: an mr compatible robot for microsurgery. In *International Congress Series*, volume 1256, pages 504–508. Elsevier.

Tada, M. and Kanade, T. (2004). Development of an mr-compatible optical force sensor. In *Engineering in Medicine and Biology Society, 2004. IEMBS'04. 26th Annual International Conference of the IEEE*, volume 1, pages 2022–2025. IEEE.

Takahashi, N., Tada, M., Ueda, J., Matsumoto, Y., and Ogasawara, T. (2003). An optical 6-axis force sensor for brain function analysis using fmri. In *Sensors, 2003. Proceedings of IEEE*, volume 1, pages 253–258. IEEE.

Tsekos, N. V., Shudy, J., Yacoub, E., Tsekos, P. V., and Koutlas, I. G. (2001). Development of a robotic device for mri-guided interventions in the breast. In *Bioinformatics and Bioengineering Conference, 2001. Proceedings of the IEEE 2nd International Symposium on*, pages 201–208. IEEE.

Tsekos, N. V., Ozcan, A., and Christoforou, E. (2005). A prototype manipulator for magnetic resonance-guided interventions inside standard cylindrical magnetic resonance imaging scanners. *Journal of biomechanical engineering*, **127**(6), 972–980.

Tsekos, N. V., Khanicheh, A., Christoforou, E., and Mavroidis, C. (2007). Magnetic resonance-compatible robotic and mechatronics systems for image-guided interventions and rehabilitation: a review study. *Annu. Rev. Biomed. Eng.*, **9**, 351–387.

Viehweg, P., Heinig, A., Amaya, B., Alberich, T., Laniado, M., and Heywang-Köbrunner, S. (2002). Mr-guided interventional breast procedures considering vacuum biopsy in particular. *European journal of radiology*, **42**(1), 32–39.

Warner, E., Plewes, D., Shumak, R., Catzavelos, G., Di Prospero, L., Yaffe, M., Goel, V., Ramsay, E., Chart, P., Cole, D., *et al.* (2001). Comparison of breast magnetic resonance imaging, mammography, and ultrasound for surveillance of women at high risk for hereditary breast cancer. *Journal of Clinical Oncology*, **19**(15), 3524–3531.

Webster III, R. J., Memisevic, J., and Okamura, A. M. (2005). Design considerations for robotic needle steering. In *Robotics and Automation, 2005. ICRA 2005. Proceedings of the 2005 IEEE International Conference on*, pages 3588–3594. IEEE.

Yang, B., Tan, U.-X., McMillan, A. B., Gullapalli, R., and Desai, J. P. (2011a). Design and control of a 1-dof mri-compatible pneumatically actuated robot with long transmission lines. *Mechatronics, IEEE/ASME Transactions on*, **16**(6), 1040–1048.

Yang, B., Tan, U.-X., McMillan, A., Gullapalli, R., and Desai, J. P. (2011b). Design and implementation of a pneumatically-actuated robot for breast biopsy under continuous mri. In *Robotics and Automation (ICRA), 2011 IEEE International Conference on*, pages 674–679. IEEE.

Zuiani, C., Mazzarella, F., Londero, V., Linda, A., Puglisi, F., and Bazzocchi, M. (2007). Stereotactic vacuum-assisted breast biopsy: results, follow-up and correlation with radiological suspicion. *La radiologia medica*, **112**(2), 304–317.